ELSEVIER

Marine Geology 229 (2006) 133 – 157

MARINE GEOLOGY
INTERNATIONAL JOURNAL OF MARINE GEOLOGY, GEOCHEMISTRY AND GEOPHYSICS

www.elsevier.com/locate/margeo

The impact of oxic alteration on plume-derived transition metals in ridge flank sediments from the East Pacific Rise

Rachel M. Dunk *,[1], Rachel A. Mills

School of Ocean and Earth Science, National Oceanography Centre, Southampton, University of Southampton, SO14 3ZH, UK

Received 17 October 2005; received in revised form 13 March 2006; accepted 20 March 2006

Abstract

We describe transition metal behaviour during early diagenesis in sediments collected along a transect across the eastern flank of the East Pacific Rise (EPR) at 14°S overlying crust with magnetic ages of 0.36 Ma to 4.6 Ma.

The sediments are lithologically simple and consist of biogenic carbonate, hydrothermal plume precipitates and minor basaltic debris. Sedimentation rates range from ~1 cm/ka in the near-axis region (0.36 Ma) to ~0.1–0.2 cm/ka across the young ridge flank (by 1.9 Ma, or within ~142 km from axis). Redox indicators (porewater $Mn(II)_{aq}$ and solid phase Mo/Mn ratios) indicate fully oxic conditions in near-axis sediments, changing to mildly suboxic conditions across the ridge flank.

Sequential extraction analysis of sediments from the 0.36 Ma site indicates that oxic alteration of Fe oxyhydroxides is dominated by transformation of ferrihydrite to goethite, implying that alteration occurs via dissolution followed by nucleation and precipitation. The extent of alteration (amorphous Fe/total plume-derived Fe) ranges from 0.3 to 0.8, and the time to half conversion is on the order of ~100 ka. V associated with plume-derived ferrihydrite is strongly discriminated against during alteration to goethite and the distribution coefficient ($D_V = (V/Fe)_{goethite}/(V/Fe)_{dissolved}$) is in the range 0.45–0.59. Cu, Zn and Ni are delivered to the sediment in association with both Fe oxyhydroxides and Mn oxides, where ~70% of Cu and Zn and ~10% of Ni are associated with Fe oxyhydroxides. The Fe-adsorbed Cu and Zn are incorporated quantitatively into the lattice structure of goethite during alteration. The Fe-associated Ni most likely represents Ni co-precipitated as Ni–Fe ferrihydrite and incorporated into goethite during alteration. Co is associated only with Mn oxides. The oxic alteration of hydrothermal Fe oxyhydroxides therefore represents a relatively permanent sink (where goethite dissolution is a prerequisite for metal release) for a maximum of ~70% of plume-derived Cu and Zn, ~50% of V, ~10% of Ni and 0% of Co. In oxic sediments, the remaining plume-derived metals are retained in association with amorphous Fe oxyhydroxides and Mn oxides, although this fraction is highly susceptible to diagenetic remobilization under suboxic conditions.

Keywords: East Pacific Rise; Nazca Plate; hydrothermal sediments; geochemistry; transition metals

1. Introduction

Sediments formed along the Mid Ocean Ridges have a distinct geochemical signature in comparison to other pelagic sediments (Bostrum et al., 1969) due to the large input of metal-rich precipitates that settle out of hydrothermal plumes (e.g. Mills and Elderfield, 1995).

* Corresponding author. Tel.: +44 1904 43 4472; fax: +44 1904 43 2516.
E-mail address: Rachel.Dunk@googlemail.com (R.M. Dunk).
[1] Present address: Department of Chemistry, University of York, Heslington, York, YO10 5DD, UK.

0025-3227/$ - see front matter © 2006 Elsevier B.V. All rights reserved.
doi:10.1016/j.margeo.2006.03.007

In addition to the rapid precipitation and deposition of vent-derived metals within the immediate vicinity of the vent (e.g. Dymond and Roth, 1988; German et al., 2002), the scavenging of dissolved seawater species by plume-derived amorphous Fe oxyhydroxides and Mn oxides, and subsequent deposition of plume particles across the ridge flanks, is thought to be an important removal mechanism in the geochemical cycling of many trace elements (e.g. Rudnicki and Elderfield, 1993). Plume-derived colloidal ferrihydrite, $Fe(OH)_3$, acts as a highly efficient sink for scavenged trace elements due to its high specific surface area (Campbell, 1991; Feely et al., 1994) and poorly crystalline Mn oxides are also available to scavenge metals from the plume or entrained seawater. In particular, positive linear correlations have been observed between plume particle-Fe and the elements P, V, Cr, As, and U which are all present in seawater as negatively charged oxyanion or carbonate species (Feely et al., 1990a,b, 1994, 1996; German et al., 1991a,b; Metz and Trefry, 1993; Trefry and Metz, 1989). Coprecipitation of the divalent transition metals (e.g. Cu, Zn, Ni, Co) with Fe oxyhydroxides has also been observed (Ford et al., 1997, 1999; Gerth, 1990; Martinez and McBride, 1998; Savenko, 2001). For many particle reactive elements, hydrothermal plume removal fluxes are as great as, or at least significant, when compared to the riverine input to the ocean (e.g. German and Von Damm, 2003). However, the net effect of hydrothermalism on geochemical budgets is also dependent on the extent to which plume-element/Fe ratios are preserved during sedimentary diagenesis, and little is yet known about the diagenetic fate of these plume-derived elements.

Sediments with the highest hydrothermal component are typically found near the rise crest, where the accumulation pattern reflects both the location of hydrothermal activity and the plume processes that disperse the hydrothermal precipitates (Dymond, 1981). Dispersion of particles from neutrally buoyant hydrothermal plumes is dominated by topographically steered flow along axis, and escape of plume material into adjacent deep basins is predicted to be minimal (<100 km off axis) except in areas where pronounced across-axis circulation occurs (Speer et al., 2003). One location where large-scale off-axis plume transport is well documented is at 2500 m water depth on the Southern East Pacific Rise (SEPR) at ~15°S (Lupton, 1995). At this latitude, the westward dispersion of hydrothermal particles leads to extreme metal enrichments in sediments to the west of the ridge and large gradients in plume input across the eastern ridge flank. Here we examine the diagenetic alteration of hydrothermal plume precipitates deposited in the EXCO (EXchange between the Crust and Ocean) study area, situated on the eastern flank of the super-fast spreading section of the SEPR at ~14°–15°S, and so determine the extent to which the plume particle signature is preserved during diagenesis.

2. Regional setting

The EXCO study area intersects the ridge axis of the SEPR at 14°14′S, 60 km to the south of the Garrett transform fault and north of a minor ridge discontinuity at 14°27′S (Fig. 1; Grevemeyer et al., 1997; Weigel et al., 1996). At 14°14′S the ridge morphology is characterised by a prominent bathymetric high with smooth flanks and a relatively flat summit (Scheirer and MacDonald, 1993). The axis is a blocky ridge crest about 300 m high and 10 km wide, where the shallowest depth of the ridge is ~2600 m (Hauschild et al., 2003). The ridge segment is magmatically active, with only minor changes in melt supply both along axis and over the last 9.3 Ma (Grevemeyer et al., 1998). Since 9.3 Ma, seafloor-spreading rates derived from magnetic data indicate a half spreading rate of the Nazca and Pacific plates of 75 mm/yr, with symmetric spreading over the last 2.7 Ma (Grevemeyer et al., 2002). Before this time, seafloor spreading was faster to the east (~86 mm/yr) than the west (~68 mm/yr) due to the migration of overlapping spreading centres transferring oceanic lithosphere from the Pacific to the Nazca plate (Grevemeyer et al., 2002). On the eastern flank, within 225 km (~3 Ma) of the spreading centre, abyssal hills and intervening valleys strike parallel to the ridge axis (013°), implying a spreading system similar to the present configuration of the ridge (Grevemeyer et al., 1997, 2002). Beyond 225 km, the seafloor fabric is oriented obliquely to the strike of the axis and a distinct change in seafloor features occurs, where this change corresponds to the change in spreading rate (Grevemeyer et al., 1997, 2002). The seafloor is roughest between 230 and 525 km offset (3–6.5 Ma) and, within this region, seamounts are more abundant and higher than elsewhere in the survey area (Grevemeyer et al., 1997).

Away from the ridge crest, the seafloor has subsided asymmetrically and reached depths of 3400–3500 m to the west and 3700–3900 m to the east by 7 Ma (Hauschild et al., 2003). On the western flank, sediment thickness (as determined from seismic reflection and sediment echo-sounding measurements) increases more or less continuously, corresponding to a constant sedimentation rate on the order of ~1 cm/ka for the

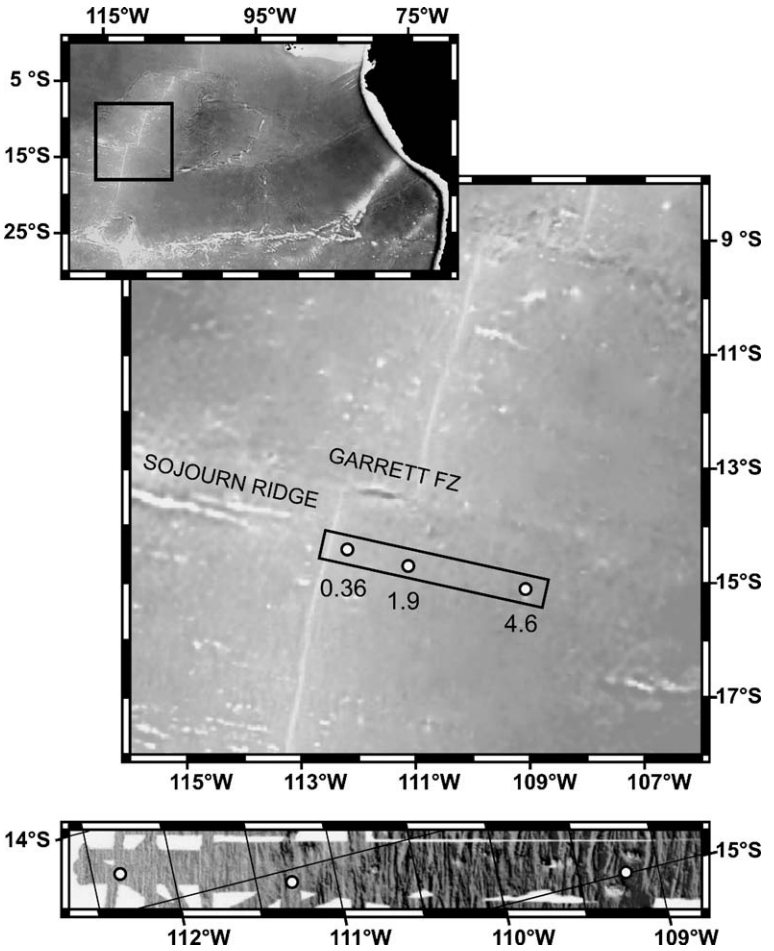

Fig. 1. The EXCO study area and location of the three sediment study sites overlying crust with magnetic ages of 0.36 Ma, 1.9 Ma and 4.6 Ma. The bottom panel shows the bathymetry along the ridge perpendicular transect.

last 7 Ma. However, on the eastern flank, sediment thickness fits the variation expected for ~1 cm/ka only for the first 2 Ma, then increases slowly with distance to ~30 m on 9 Ma crust, corresponding to a sedimentation rate of less than 0.2 cm/ka (Hauschild et al., 2003). Seismic records that reflect the volcanic topography beneath the sediments show that on the eastern flank sediments are draping the basement rather than ponding, implying that sediment has been accumulated from particles settled from suspension, and that neither significant syn-depositional or post-depositional sediment redistribution has occurred (Hauschild et al., 2003).

The principal sediment component along the SEPR is biogenic, commonly calcareous, ooze, and the non-biogenic component is dominated by hydrothermal plume fall-out (Dymond, 1981). As the EXCO study area is somewhat removed from the zone of high surface water productivity in the eastern equatorial Pacific, the input of organic matter to these sediments is low. Similarly, detrital material of continental origin is negligible due to the distal location of the SEPR with respect to continental landmasses, although near the ridge axis the detrital component is significant and variable due to local contributions of exposed basaltic basement (Dymond, 1981; Marchig et al., 1986). The hydrothermal plume input represents the dominant source of Fe and trace elements to Nazca Plate sediments along the SEPR (Dymond, 1981; Heath and Dymond, 1977, 1981). Although there is no known vent field at 14°–15°S, an extensive survey of plume particulates along the super-fast spreading section of the SEPR revealed almost continuous venting from 13° to 19°S (RIDGEFLUX; Feely et al., 1996). While the large δ^3He plume extends westward of the SEPR at this latitude, there is a clear expression of the ^{3}He anomaly to the east of the rise crest in this region (WOCE line P18 at a longitude of 105°W), and the eastern flank

underlies the largest gradient in plume supply in the global ridge system (Lupton, 1995). Hence ridge crest cores are subject to intense plume activity and the known plume trajectory allows sampling along a transect perpendicular to the flow regime to an area of lower plume input. The EXCO study area therefore represents an ideal location in which to study the composition and early diagenesis of hydrothermal sediments within a lithologically simple system.

3. Materials and methods

3.1. Sample collection

This research focuses on eight cores collected during *R/V Sonne* cruise 145/2 in 2000 (EXCOII/2) in a transect across the eastern flank of the EXCO study area from locations overlying crust with estimated ages of 0.36 Ma, 1.9 Ma and 4.6 Ma (Fig. 1 and Table 1). The bathymetry at the two younger sites is characterized by lines of abyssal hills forming a series of ridges that run parallel to the strike of the ridge crest (013°). At the 0.36 Ma site, three cores are situated along the crest of an abyssal hill ridge (E12, E18, E19) and one is situated in an adjacent valley (E17). At the 1.9 Ma site, 2 cores are situated on a ridge (E20, E24) and one on the ridge flank toward the adjacent valley (E10). The 4.6 Ma site is in the vicinity of two medium to large sized seamounts aligned approximately parallel to the ridge axis, where core E7 is located on level basement between the two seamounts. A gravity corer fitted with a 6-m barrel was used to collect all cores, recovering sediment thicknesses of 3.28–5.75 m.

The cores were split and sampled aboard ship. Sediment and associated porewater samples were collected from 2 to 5 cm sections of undisturbed sediment (7–15 samples per core). Porewaters were extracted by centrifugation under refrigerated conditions (4 °C) and filtration of the supernatant liquor through a 0.45-μm filter. All samples were stored under refrigerated conditions (4 °C) prior to analysis. Porewater Mn was determined by ICP–AES with a detection limit of ca. 0.1 μmol/kg.

Table 1
Location, depth, and total core recovery of *R/V Sonne* SO145/2 (EXCOII/2) cores collected in transect from the SEPR axis across the Nazca plate

Crustal age (Ma)	Distance to axis (km)	Core I.D.	Latitude (S)	Longitude (W)	Depth (m)	Core recovery (cm)
0.36	27	E12	14°16.48′	112°19.38′	3047	430
		E17	14°16.88′	112°19.84′	3089	382
		E18	14°16.73′	112°19.44′	3061	468
		E19	14°16.54′	112°19.44′	3043	328
1.9	142	E10	14°33.67′	111°15.20′	3190	575
		E20	14°34.30′	111°17.10′	3239	575
		E24	14°33.75′	111°14.79′	3184	575
4.6	366	E7	14°58.29′	109°12.90′	3733	570

Splits of all sediment samples from cores E12 (0.36 Ma site), and E10 (1.9 Ma site), were wet sieved to allow size fractionated (0–125 μm, 125–500 μm, >500 μm) microscopic inspection of the sediments. Sediment samples of known volume were also collected from undisturbed sections of the core immediately adjacent to the primary samples to allow determination of porosity and dry bulk density.

3.2. Geochemical analysis

Dried, ground sediment samples were submitted to a three step digestion protocol (aqua regia (3:1 HCl/HNO_3); $HClO_4$ and HF (3:4); $HClO_4$), evaporated to dryness and dissolved in 0.6 M HCl. The concentrations of Ca, Al, Ti, Fe, Mn, Mo, V, Cu, Zn, Ni, and Co were determined by ICP–AES, for which the instrument was calibrated using matrix matched standards. Five replicate measurements gave relative standard deviations generally better than 2% and always better than 5%, except for Co (<10%) and Mo (only data with a relative standard deviation of <10% are presented). The precision and accuracy of the entire digest and analytical procedure was determined through 6 replicate digests of the US Geological Survey MAG-1 standard, which gave excellent agreement to certified values and precisions better than 2%, with the exception of Cu (5%) and Mo. For Mo, the MAG-1 concentration was below the analytical detection limit (~1 ng/g in digest solution ≈ 1 μg/g in solid phase), and lower than the reported value (1.6 μg/g). We therefore consider the reported Mo concentrations to be minimum values.

A sequential extraction (partition analysis) was carried out on a subset of 9 samples from core E12 at the 0.36 Ma site to separate the sediment into four fractions: (1) CAE (carbonate, adsorbed or readily exchangeable species, 10% acetic acid); (2) AM (acid reducible 'amorphous' Fe oxyhydroxides and Mn oxides, 1 M hydroxylamine hydrochloride in 25% acetic acid); (3) ORG (organic material, 5% hydrogen peroxide); and (4) RES (residual material including crystalline Fe oxyhydroxides, as bulk digest above). The method used was that described by Bayon et al. (2002) with the following modifications: (1) the solid sample was retained in the centrifuge bottle throughout the procedure to eliminate loss during transfer steps; (2) the

conditions for the AM leach were changed to 4 h at room temperature (cf. Chester and Hughes, 1967). All fractions were brought into solution in 0.6 M HCl and analyzed as above. Sample recovery was assessed by comparison to the bulk sediment digest data, where the sum of an element concentration across the four fractions ($X_{SUM}=X_{CAE}+X_{AM}+X_{ORG}+X_{RES}$) was generally within 10% of the bulk sediment concentration (X_{bulk}). Some sample loss due to effervescence and spitting during the drying down of the AM fraction was observed for four samples (E12#4–6, E12#12). Given the excellent agreement between X_{SUM} and X_{bulk} for the remaining samples (±5%), the AM fraction was also determined by difference for the transition elements Fe, Mn, V, Cu, Ni, and Co. The Zn data were not of sufficient quality to justify this approach, as Zn_{SUM} was significantly in excess of Zn_{bulk} (>10%), most likely due to contamination of Zn at low concentrations.

All element data were corrected for the mass contribution in each sample resulting from the precipitation of porewater salts.

X-ray diffraction (XRD) analyses of the bulk sediment samples and the RES fraction from core E12 were carried out on a Phillips PW automated powder diffractometer using Co-Kα radiation ($\lambda=7.18897$ Å). Dry powder mounts were scanned between a 2θ of 3° to 76° at intervals of 0.002° and a scan rate of 0.2°/min. The detection limit for all minerals was ca. 1%.

4. Results

4.1. Core lithology

Three cores collected at the 0.36 Ma site (E12, E17, and E19) appear to have reached basement; where these cores produced severely dented core cutters, and fragments of glass and basement rock were recovered from the core catcher and/or in the lower section of the core.

No hiatuses were observed in the cores collected from the 0.36 and 1.9 Ma sites, consistent with the accumulation of sediments settling locally from suspension (Hauschild et al., 2003). However, two distinct graded beds of well-sorted sediment defined by sharp contacts at the base were observed at depths of 255–220 cmbsf and 100–55 cmbsf in the core from the 4.6 Ma site, suggesting that at least one sixth of material accumulated there was initially deposited on the flanks of the adjacent seamounts and transported to the core site by mass flow events.

A general trend of decreasing sediment porosity with increasing age of site, and thus water depth and pressure, was observed, with mean porosities of 76% at the 0.36 Ma site, 72% at the 1.9 Ma site and 66% at the 4.6 Ma site. For all the cores at the 0.36 Ma site the highest porosity of 79–81% occurred at mid-depths of 140–170 cmbsf, corresponding to a dark brown/black Fe–Mn-rich, foram-poor sediment layer.

Based on microscopic inspection and bulk sediment XRD analysis, the EXCO sediments consist of a calcitic nannofossil and foraminiferal ooze with secondary Fe oxyhydroxides and Mn oxides, and basaltic fragments in some samples. The dominant hue of the calcareous ooze varies from pale cream to very dark brown primarily due to changes in the concentration of Fe oxyhdroxides and Mn oxides. Microscopic examination of sediments from the 0.36 Ma site allowed identification of the following Fe and Mn phases: (1) amorphous Fe oxyhydroxides and Mn oxides occurring as fine grained discrete particles and coatings on foraminifera; (2) combined ferromanganese phases such as mixed colloidal aggregates, infilling of foraminifera tests and micro-nodules (<500 μm in diameter); (3) discrete masses of black Mn oxides; (4) discrete masses of goethite; and (5) minor haematite. XRD analysis of the RES fraction confirmed the presence of goethite, and the additional minor phases of opaline silica, barite, and a clay mineral (Fig. 2).

4.2. Sediment composition

The major element and transition metal contents of the bulk sediment are presented in Table 2. Potential phase tracers (Ca, Al, Ti, Fe, Mn) for the three principal sediment phases identified above (calcium carbonate, detrital material, and Fe oxyhydroxides and Mn oxides) were chosen with reference to previous geochemical studies in this area and the sequential extraction data. The mean partitioning of the tracer elements between the sequential extraction fractions is shown in Fig. 3.

4.2.1. Carbonate input

The sediment calcium carbonate contents were determined by correcting the ICP–AES data for detrital Ca (see Eqs. (2) and (3), and Table 3) and calculating for $CaCO_3$ (Dymond, 1981; Dymond et al., 1976). This approach is justified by the sequential extraction data, which demonstrates that ~99% of Ca resides in the CAE fraction (Fig. 3). The calculated carbonate contents, expressed as weight percent of the bulk sediment (wt. %), are presented in Table 4.

4.2.2. Detrital input

Previous studies in this region have used Al as the detrital phase tracer (Dymond, 1981; Marchig et al.,

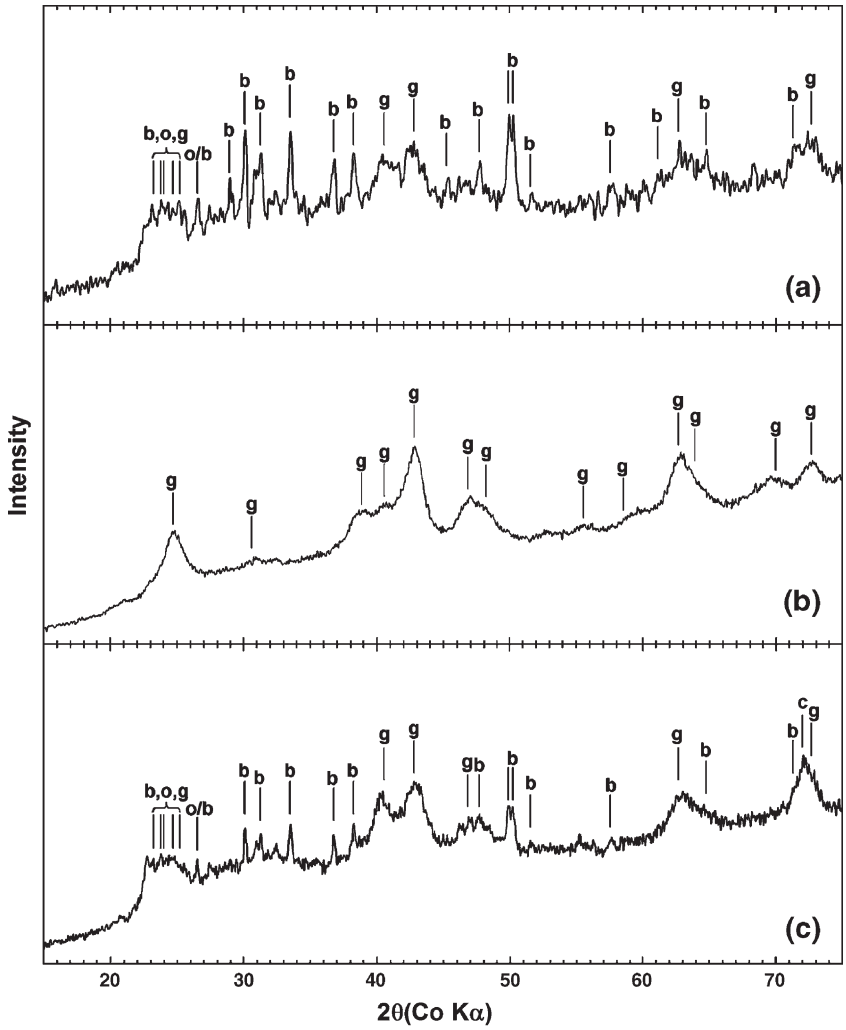

Fig. 2. XRD patterns of the residual (RES) fraction of 0.36 Ma site sediments, showing the presence of barite (b), opaline silica (o), goethite (g) and a clay mineral (c). (a) E12#4, 63.5 cmbsf; (b) E12#7, 165 cmbsf; (c) E12#9, 270.5 cmbsf.

1986). However, in regions of low detrital input, such as the equatorial Pacific, a significant proportion of the total sediment Al may have been scavenged from seawater (e.g. Murray and Leinen, 1996). Detrital material is relatively refractory and should fall within the RES fraction of the sequential extraction. In the EXCO sediments, only ~45% (range 30–60%) of total Al resides in the RES fraction, with up to 30% occurring in the labile CAE fraction (Fig. 3). Conversely, Ti was found almost exclusively in the RES fraction (Fig. 3), and was therefore selected as the detrital phase tracer. If it is assumed that the dominant source of detrital material to the EXCO sediments is locally sourced basaltic debris, and that the majority of weathering reactions occur within the sediment column, then Ti can be employed as a reliable tracer of the detrital phase using Eq. (1):

$$\text{Detrital (wt.\%)} = \text{Ti}_{\text{bulk}}/(100^{*}[\text{Ti}]_{\text{basalt}}) \quad (1)$$

where Ti_{bulk} is the Ti concentration of the bulk sediment in μg/g and $[\text{Ti}]_{\text{basalt}}$ is the Ti content of the basaltic detritus in wt.%. The mean Ti content and element/Ti ratios of basalts collected from the EXCO study area are presented in Table 3 (after data of Grevemeyer et al., 2002 and Schramm et al., 2005). The calculated detrital content of the sediments are presented in Table 4.

The detrital contribution of Ca, Fe and Mn (X_{detrital}), and the corrected 'excess' bulk sediment

Table 2
Bulk sediment element concentrations at the (a) 0.36 Ma, (b) 1.9 Ma, and (c) 4.6 Ma sites

Sample I.D.	cmbsf	Ca (mg/g)	Al (mg/g)	Ti (μg/g)	Fe (mg/g)	Mn (mg/g)	Mo (μg/g)	V (μg/g)	Cu (μg/g)	Zn (μg/g)	Ni (μg/g)	Co (μg/g)
(a) 0.36 Ma site												
E12#1	4.0	362	0.72	58.2	29.5	9.0		68.4	130	53.1	70.4	19.0
E12#2	19.0	327	0.93	89.0	52.2	15.2		127	206	83.2	113	22.8
E12#3	34.5	357	1.02	96.0	40.1	9.5		86.4	117	49.0	70.4	15.6
E12#4	63.5	374	0.95	80.4	33.4	8.9		73.9	112	45.2	66.1	22.2
E12#5	82.5	380	0.95	89.4	32.4	8.4		70.3	114	45.7	69.5	17.0
E12#6	118.5	369	1.41	177	34.3	9.2		76.2	136	51.0	76.7	19.3
E12#7	165.0	259	1.68	204	121	38.4	44.1	372	593	227	192	38.0
E12#8	219.0	357	2.31	308	36.2	7.9		83.8	112	47.2	63.5	16.8
E12#9	270.5	346	3.14	393	44.3	12.2	15.9	122	195	73.8	93.3	24.2
E12#10	325.5	324	3.59	545	57.6	16.0	31.0	177	195	97.9	103	18.8
E12#11	367.5	296	5.52	752	74.3	14.0	17.4	180	258	122	110	15.1
E12#12	405.0	318	4.15	585	65.6	14.6	24.4	181	271	121	124	18.2
E17#1	3.5	373	0.77	63.5	31.4	9.6		73.8	139	66.2	74.1	18.8
E17#2	19.0	340	0.93	87.9	53.8	15.7		131	215	91.1	112	24.8
E17#3	50.5	357	0.93	84.5	35.9	9.3		82.1	127	49.5	73.3	18.1
E17#4	94.5	347	1.56	199	41.0	10.5		92.5	163	60.3	100	21.5
E17#5	148.5	258	1.79	204	123	38.6	58.9	378	611	239	205	39.3
E17#6	225.0	340	2.57	318	48.6	13.7	23.9	121	228	80.1	125	20.9
E17#7	278.5	293	3.33	465	86.4	27.6	57.2	252	432	175	195	26.6
E18#1	5.5	357	0.76	62.5	33.0	9.9		74.8	142	66.5	76.5	11.3
E18#2	17.0	329	0.99	95.0	54.0	15.4		133	209	93.5	112	14.8
E18#3	52.0	355	0.92	79.4	33.4	8.9		73.0	112	52.5	64.5	9.3
E18#4	90.5	348	1.56	181	42.2	10.3		92.7	157	64.5	89.3	12.7
E18#5	141.0	270	1.96	212	110	34.1	29.0	321	539	211	197	30.7
E18#6	180.0	344	1.45	157	42.7	8.9		99.9	125	61.1	70.2	10.2
E18#7	237.0	321	2.76	361	56.0	17.0		156	260	100	142	15.1
E19#1	11.0	364	0.75	62.0	32.1	9.7		75.0	140	62.7	76.6	14.0
E19#2	26.5	333	1.02	96.7	50.4	13.9		118	183	83.3	105	15.8
E19#3	54.5	361	0.91	78.7	32.9	8.7		69.8	112	42.5	67.3	11.7
E19#4	100.5	351	1.38	185	31.8	8.5	9.6	69.0	127	45.6	73.3	12.0
E19#5	143.5	258	1.79	183	121	38.3	80.3	357	623	236	248	35.9
E19#6	211.5	332	3.42	531	46.7	10.1	14.0	97.1	158	68.1	87.2	13.9
E19#7	237.0	331	2.82	350	52.0	15.9	29.4	135	245	87.3	134	16.3
E19#8	299.5	323	3.70	514	66.6	17.1	37.2	182	224	105	106	18.7
(b) 1.9 Ma site												
E10#1	7.0	364	0.79	44.1	6.8	2.2		13.1	42.1	32.2	28.5	9.94
E10#2	19.5	368	0.80	46.4	8.1	2.8		15.6	49.9	24.3	28.0	10.3
E10#3	59.5	376	0.68	39.7	6.7	2.1		12.4	34.9	16.0	20.6	7.82
E10#4	101.5	382	0.67	39.4	7.8	2.8		15.0	51.3	19.6	31.1	9.60
E10#5	145.0	378	1.27	69.2	22.7	6.9	8.6	47.9	105	44.5	61.8	13.2
E10#6	202.5	355	1.22	68.1	21.8	6.4	10.7	45.8	99.4	40.1	57.9	11.1
E10#7	248.0	358	0.72	47.9	17.3	5.1	11.3	37.9	70.2	38.0	49.1	7.62
E10#8	308.5	354	0.86	56.4	20.7	7.8	5.3	49.6	102	41.6	65.9	9.58
E10#9	401.0	341	0.82	59.7	32.5	11.3	5.4	86.3	125	57.1	86.4	10.4
E10#10	452.5	341	0.76	55.9	33.6	11.9	4.6	90.2	137	58.6	85.9	9.79
E10#11	503.0	344	0.75	48.0	22.3	8.2		53.7	101	42.6	71.0	8.75
E20#1	4.5	385	0.94	53.8	9.0	2.9		18.8	52.9	21.9	31.6	12.9
E20#2	19.0	395	0.85	49.1	10.2	3.4		22.1	58.9	23.8	33.7	14.0
E20#3	38.5	356	0.78	48.2	18.4	5.9	4.7	46.8	89.7	40.9	49.5	13.5
E20#4	82.5	396	0.80	45.9	10.1	3.4		21.6	60.2	23.2	33.9	12.1
E20#5	142.5	362	0.92	52.4	17.2	5.4	4.1	38.7	87.6	34.2	50.5	11.8
E20#6	186.5	372	1.30	72.6	20.7	6.5	4.5	40.4	98.5	38.5	59.0	13.4
E20#7	248.5	369	1.21	71.1	29.3	8.4	5.3	60.8	132	52.5	68.2	12.8
E20#8	322.5	378	0.81	51.5	20.4	6.5	4.0	48.8	102	61.2	53.6	10.3

(continued on next page)

Table 2 (*continued*)

Sample I.D.	cmbsf	Ca (mg/g)	Al (mg/g)	Ti (μg/g)	Fe (mg/g)	Mn (mg/g)	Mo (μg/g)	V (μg/g)	Cu (μg/g)	Zn (μg/g)	Ni (μg/g)	Co (μg/g)
E20#9	415.0	341	0.72	54.3	38.6	13.7	6.4	108	162	66.7	93.6	12.4
E20#10	446.0	372	0.77	55.1	34.3	12.3	6.3	95.3	155	64.7	90.8	13.1
E20#11	520.5	334	1.16	88.8	45.9	15.8	6.6	120	207	82.7	118.9	24.5
E20#12	553.5	350	0.93	65.6	38.3	11.5	6.3	95.7	124	64.4	85.7	13.1
E24#1	2.5	387	0.76	42.0	8.7	2.8		18.2	52.7	33.6	30.6	21.5
E24#2	14.5	387	0.72	43.8	14.4	4.8	3.7	32.0	73.0	35.5	39.0	
E24#3	42.5	399	0.75	40.0	6.3	1.9		11.4	33.3	16.5	20.5	17.6
E24#4	85.5	386	0.64	37.2	8.8	2.9		17.0	51.6	25.9	30.1	14.5
E24#5	133.5	372	1.17	66.5	17.7	5.7	6.4	36.8	89.6	37.1	61.5	13.5
E24#6	186.5	369	1.03	58.1	21.6	10.2	4.7	45.8	92.8	48.6	65.7	14.7
E24#7	256.5	362	0.72	45.4	17.5	6.8		38.1	74.0	36.5	51.9	11.4
E24#8	318.5	373	0.76	49.6	20.9	8.6	2.8	48.8	96.8	41.3	56.7	12.0
E24#12	545.5	359	0.70	47.2	29.9	10.1		68.1	126	53.2	66.7	11.4
(c) 4.6 Ma site												
E7#1	9.0	400	2.55	140	7.3	3.0		12.2	69.6	18.8	57.6	28.3
E7#2	19.0	399	2.21	120	6.2	2.5		10.2	63.0	16.6	49.7	26.3
E7#3	33.0	378	3.79	205	11.9	4.7		19.6	110	29.1	92.3	41.6
E7#4	62.5	390	2.38	131	10.0	3.6		18.7	85.1	23.4	62.4	23.2
E7#5	74.5	403	1.81	104	8.5	3.0	11.7	17.8	71.3	20.8	52.9	19.5
E7#6	109.5	367	4.01	209	14.2	5.3		22.6	132	33.7	87.8	42.1
E7#7	159.0	391	1.34	64.8	4.4	1.4		6.0	57.3	12.9	24.5	22.5
E7#8	207.0	387	2.11	103	7.5	2.6		12.4	73.8		66.9	21.9
E7#9	270.0	378	2.60	136	10.5	3.5		18.6	89.4	22.8	59.1	26.4
E7#10	310.5	400	1.80	98.4	11.5	3.8	15.5	25.2	96.0	25.5	62.1	31.9
E7#11	364.0	378	2.16	171	25.3	8.9	31.8	61.8	196	63.0	184	35.8
E7#12	412.5	346	2.99	232	33.8	11.7	41.4	81.7	260	81.0	231	46.5
E7#13	471.5	376	1.77	112	16.8	5.9	21.0	36.5	145	45.5	115	29.0
E7#14	515.5	391	1.25	83.2	13.8	4.8	19.2	31.0	99.9	33.2	62.1	23.8
E7#15	552.0	391	1.34	87.1	15.5	5.5	18.8	35.7	119	39.9	82.7	31.7

contents (X_{ex}), were estimated from Eqs. (2) and (3):

$$X_{detrital} = Ti^{*}_{bulk}(X/Ti)_{basalt} \quad (2)$$

$$X_{ex} = X_{bulk} - X_{detrital} \quad (3)$$

where $X_{detrital}$ refers to element X in the detrital phase in units of mg X per g of bulk sediment, X_{bulk} is the concentration of X in the bulk sediment (mg/g), and $(X/Ti)_{basalt}$ is the mean basaltic element/Ti ratio (wt/wt).

4.2.3. Fe oxyhydroxide and Mn oxide input

Hydrothermal plume fall-out in the far field consists dominantly of Fe oxyhydroxides and Mn oxides,

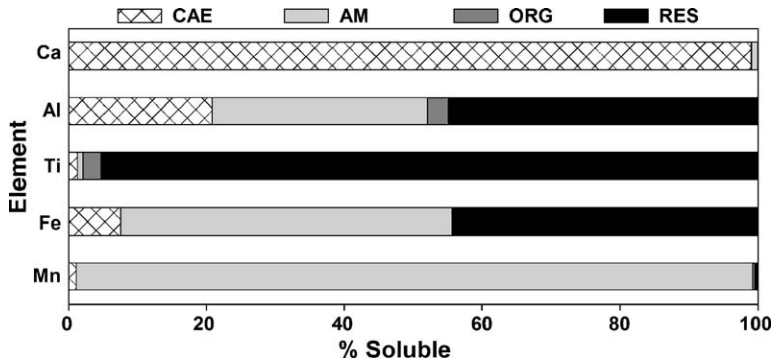

Fig. 3. Tracer element partitioning in calcitic sediments adjacent to the SEPR (0.36 Ma site) indicating the mean percentage of each element present in four fractions (1) CAE, carbonate, adsorbed and exchangeable; (2) AM, amorphous Fe oxyhydroxides and Mn oxides; (3) ORG, organic; (4) RES, residual including crystalline Fe oxyhydroxides.

Table 3
Basalt composition in the EXCO study area

Site		Ti (wt.%)	Ca/Ti (wt/wt)	Al/Ti (wt/wt)	Fe/Ti (wt/wt)	Mn/Ti (wt/wt)
0.36 and 1.9 Ma[a]	Mean (n=9)	0.88	10.5	10.1	10.5	0.19
	1σ	0.30	4.7	5.1	3.4	0.06
4.6 Ma[b]	Mean (n=8)	0.75	12.4	11.0	10.5	0.20
	1σ	0.22	3.0	2.8	1.4	0.03

[a] Mean composition of basalts aged less than or equal to 2.7 Ma, the time of the spreading rate change (data of Schramm et al., 2005).
[b] Mean composition of basaltic fragments recovered from sediment cores collected at the 4.6 Ma site (data of Grevemeyer et al., 2002).

therefore the combined use of Fe_{ex} and Mn_{ex} should provide the best tracer of this phase. The composition of the hydrothermal end-member was estimated from the most metal-rich sediments at the 0.36 Ma site, corresponding to those samples collected within the dark brown/black high porosity, Fe–Mn-rich layer occurring at a depth of ~140–170 cmbsf (E12#7, E17#5, E19#5). The assumption is made that the composition of these sediments can be accurately described by the sum of the three principal components (Metz et al., 1988):

$$100 = \text{Carbonate (wt.\%)} + \text{Detrital (wt.\%)} + \text{Hydrothermal (wt.\%)} \quad (4)$$

This assumption is supported by the XRD analysis of the RES fraction of E12#7, which demonstrated that this sediment horizon does not contain the minor phases of barite, opaline silica, or clay (Fig. 2b). The Fe and Mn content of the carbonate phase is assumed to be zero, thus the hydrothermal contribution of these elements to the bulk sediment composition is equal to X_{ex} (mg per g bulk sediment) and the concentrations of Fe and Mn within the hydrothermal phase ($[X]_{hydrothermal}$ in wt.%) are determined from:

$$[X]_{hydrothermal} = 10{*}X_{ex}/(100 - \text{Carbonate (wt.\%)} - \text{Detrital (wt.\%)}) \quad (5)$$

Giving a mean hydrothermal end-member composition of 35.5±0.4 wt.% Fe and 11.4±0.1 wt.% Mn (Fe_{ex}/Mn_{ex}=3.1). The contribution of hydrothermal material to the bulk composition of the EXCO sediments can then be estimated from:

$$\text{Hydrothermal (wt.\%)} = 10{*}X_{ex}/[X]_{hydrothermal} \quad (6)$$

The calculated hydrothermal contents of all samples are presented in Table 4.

4.2.4. Transition metals

The Mn_{ex}, V, Cu, Zn, Ni and Co data plotted against Fe_{ex} for all sites are shown in Fig. 4. Linear relationships are observed between Fe_{ex} and Mn_{ex}, V, Cu and Zn, although the sediments at the 4.6 Ma site appear to be moderately enriched in Cu with respect to the two younger sites. Both Ni and Co also show this differential relationship to Fe_{ex} across the EXCO study area, with higher ratios observed at the 4.6 Ma site. In general, the Ni data show a strong covariance with Fe_{ex}, although some departures from a linear trend are observed, particularly at the 0.36 Ma site where samples with a high Fe_{ex} content deviate toward low Ni. The Co data do not show a strong relationship to Fe_{ex}, although a general trend of increasing Co with increasing Fe_{ex} is observed.

The down-core speciation of these trace metals at the 0.36 Ma site (as determined by the sequential extraction of sediments from core E12) are presented in Fig. 5 in comparison to that of Fe_{ex}. The RES fraction for Fe and Mn are corrected for the detrital contribution.

5. Discussion

5.1. Sediment redox status

The major control on sediment redox status along the SEPR is the latitudinal gradient in export production away from the high productivity eastern equatorial Pacific to the low productivity oligotrophic gyre at ~15°S (Smith et al., 1997). This gradient in carbon export is manifest as a decreasing trend in opaline silica and refractory biogenic material with latitude in Nazca Plate sediments (Dymond, 1981).

The EXCO study area underlies a region of low primary production and high bottom water oxygen concentrations (130–140 μmol/kg; WOCE Line P18). Organic carbon in the sediments is low, decreasing from 0.2 to 0.3 wt.% in the upper 20 cm at the 0.36 Ma site to values of ~0.1 wt.% at depth (Dunk, 2004). This is consistent with a minor input of organic material, where labile carbon is oxidized in surface sediments by free oxygen within the porewater (Wilson et al., 1985), and suggests that postdepositional reductive remobilization of elements during early diagenesis is minimal.

Table 4
Bulk sediment composition at the (a) 0.36 Ma, (b) 1.9 Ma, and (c) 4.6 Ma sites

Sample I.D.	Carbonate (wt.%)	Detrital (wt.%)	Hydrothermal (wt.%)	Total (wt.%)
(a) 0.36 Ma site				
E12#1	90.2	0.7	8.1	99.0
E12#2	81.4	1.0	14.4	96.9
E12#3	88.8	1.1	11.0	100.9
E12#4	93.1	0.9	9.2	103.1
E12#5	94.6	1.0	8.9	104.5
E12#6	91.8	2.0	9.1	102.9
E12#7	64.1	2.3	33.6	100.0
E12#8	88.3	3.5	9.3	101.0
E12#9	85.5	4.5	11.3	101.2
E12#10	79.5	6.2	14.6	100.3
E12#11	72.0	8.5	18.7	99.3
E12#12	77.8	6.6	16.8	101.2
E17#1	92.9	0.7	8.7	102.3
E17#2	84.7	1.0	14.9	100.6
E17#3	88.9	1.0	9.9	99.7
E17#4	86.1	2.3	11.0	99.3
E17#5	64.0	2.3	34.1	100.4
E17#6	84.2	3.6	12.7	100.5
E17#7	72.0	5.3	23.0	100.3
E18#1	88.9	0.7	9.1	98.7
E18#2	82.0	1.1	14.9	98.0
E18#3	88.4	0.9	9.2	98.5
E18#4	86.4	2.1	11.3	99.8
E18#5	66.8	2.4	30.4	99.6
E18#6	85.6	1.8	11.6	99.0
E18#7	79.3	4.1	14.7	98.1
E19#1	90.7	0.7	8.9	100.2
E19#2	82.8	1.1	13.9	97.8
E19#3	90.0	0.9	9.0	99.9
E19#4	87.1	2.1	8.4	97.6
E19#5	64.1	2.1	33.6	99.7
E19#6	81.4	6.0	11.6	99.0
E19#7	81.7	4.0	13.6	99.3
E19#8	79.2	5.8	17.3	102.3
0.36 Ma site average				100.0±1.6
(b) 1.9 Ma site				
E10#1	90.8	0.5	1.8	93.1
E10#2	91.7	0.5	2.2	94.4
E10#3	93.8	0.5	1.8	96.0
E10#4	95.3	0.4	2.1	97.9
E10#5	94.3	0.8	6.2	101.3
E10#6	88.6	0.8	5.9	95.3
E10#7	89.3	0.5	4.7	94.6
E10#8	88.3	0.6	5.7	94.6
E10#9	85.1	0.7	9.0	94.8
E10#10	85.1	0.6	9.3	95.0
E10#11	85.7	0.5	6.1	92.4
E20#1	96.0	0.6	2.4	99.0
E20#2	98.4	0.6	2.7	101.7
E20#3	88.9	0.5	5.0	94.5
E20#4	98.6	0.5	2.7	101.9
E20#5	90.4	0.6	4.7	95.7
E20#6	92.7	0.8	5.6	99.1
E20#7	92.0	0.8	8.0	100.8
E20#8	94.2	0.6	5.6	100.4
E20#9	84.9	0.6	10.7	96.2
E20#10	92.9	0.6	9.5	103.0
E20#11	83.1	1.0	12.7	96.8
E20#12	87.2	0.7	10.6	98.5
E24#1	96.6	0.5	2.3	100.8
E24#2	96.5	0.5	3.9	100.8
E24#3	99.4	0.4	1.7	101.5
E24#4	96.4	0.8	2.4	99.5
E24#5	92.7	0.7	4.8	98.2
E24#6	92.0	0.5	5.9	98.4
E24#7	90.2	0.6	4.8	95.5
E24#8	93.1	0.5	5.7	99.3
E24#12	89.6	0.5	8.3	98.4
1.9 Ma site average				97.7±2.9
(c) 4.6 Ma site				
E7#1	99.6	1.9	1.6	103.1
E7#2	99.1	1.6	1.4	102.1
E7#3	93.7	2.7	2.7	99.2
E7#4	97.1	1.7	2.4	101.2
E7#5	100.3	1.4	2.1	103.8
E7#6	91.0	2.8	3.4	97.1
E7#7	97.4	0.9	1.1	99.3
E7#8	96.3	1.4	1.8	99.5
E7#9	93.9	1.8	2.6	98.2
E7#10	99.7	1.3	3.0	104.0
E7#11	93.7	2.3	6.6	102.7
E7#12	85.6	3.1	8.8	97.5
E7#13	93.6	1.5	4.4	99.5
E7#14	97.4	1.1	3.6	102.2
E7#15	97.4	1.2	4.1	102.7
4.6 Ma site average				100.8±2.3

In oxygen depleted regimes, solid phase Mn(IV) and Fe(III) are reduced and mobilized as dissolved $Mn(II)_{aq}$ and $Fe(II)_{aq}$. The Mn(IV)/Mn(II) transition occurs at higher Eh than the Fe(III)/Fe(II) transition. Post depositional separation of Fe and Mn can therefore occur via reductive remobilization of Mn during early organic carbon diagenesis (Froelich et al., 1979). At the 0.36 Ma site, porewater $Mn(II)_{aq}$ was below the analytical detection limit (<0.1 μmol/kg) in all samples except E17#6 (211 cmbsf, 0.9 μmol/kg) and E18#2 (17 cmbsf, 0.8 μmol/kg). At the 1.9 Ma site, $Mn(II)_{aq}$ was below the detection limit in core E20. Surface sediments in cores E10 and E24 also showed undetectable $Mn(II)_{aq}$, although below 200 cmbsf, significant porewater $Mn(II)_{aq}$ was observed (4 and 16 μmol/kg, respectively), indicating suboxic conditions at depth in these cores. Core E7 at the 4.6 Ma site has a relatively constant downcore $Mn(II)_{aq}$ of ~6 μmol/kg.

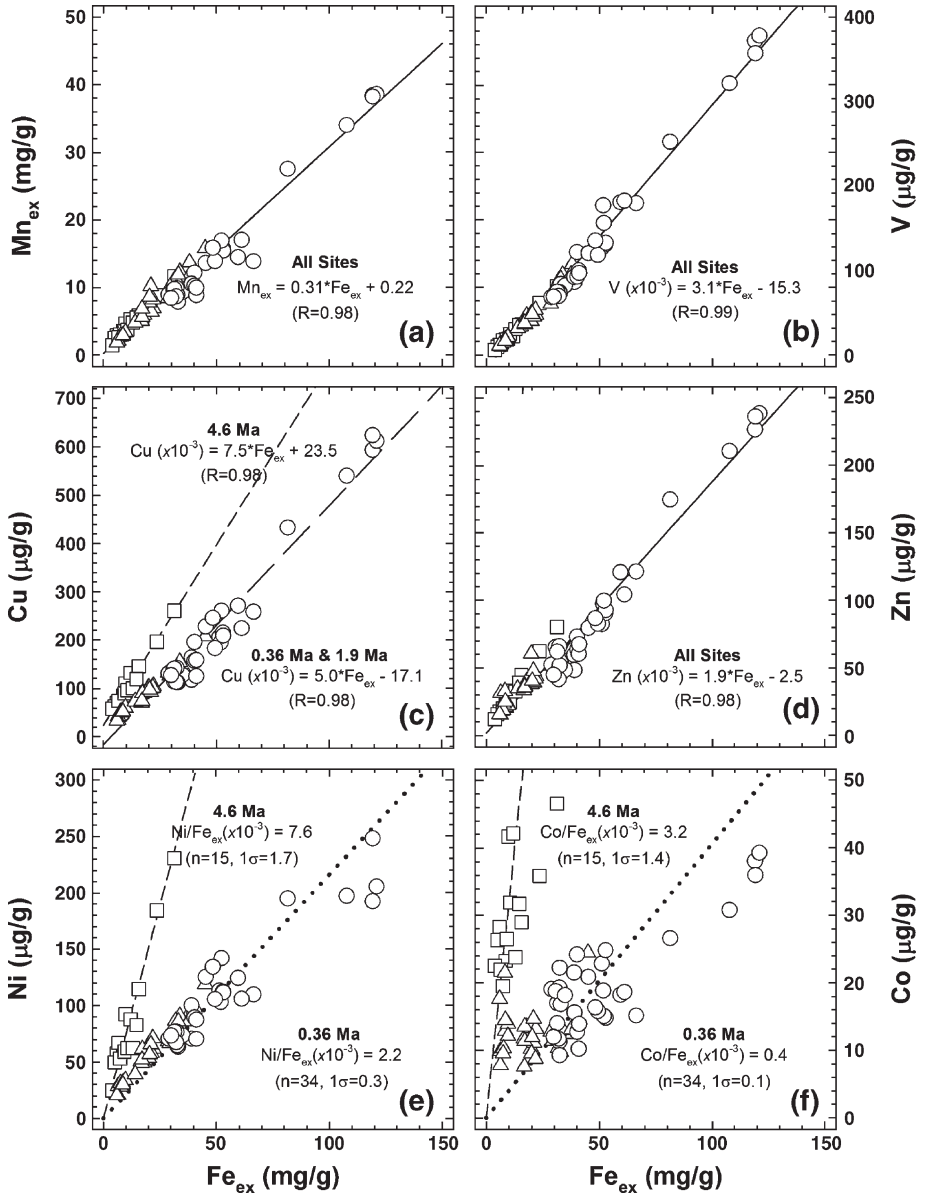

Fig. 4. The transition metals (a) Mn_{ex} (b) V (c) Cu (d) Zn (e) Ni and (f) Co vs. basalt corrected Fe (Fe_{ex}) for all sites (circles = 0.36 Ma Site, triangles = 1.9 Ma Site, squares = 4.6 Ma site). For (a) to (d): lines given show the type II (geometric mean) regressions of the data. For (e) and (f): lines give the mean transition metal/Fe_{ex} ratio.

The solid phase Mn_{ex} data are plotted against Fe_{ex} for all sites in Fig. 4a. The mean Fe_{ex}/Mn_{ex} of this data set is 3.1 ± 0.6 (1σ, n = 81), and a model II (geometric mean) linear regression gives an Fe_{ex}/Mn_{ex} ratio of 3.3 (R = 0.98). This is in excellent agreement with previously observed values in oxic sediments along the SEPR at 18.5°S (3.3 ± 0.5; Marchig et al., 1986) and 20°S (3.1 ± 0.3; Shimmield and Price, 1988) and is consistent with fall-out from a relatively aged neutrally buoyant plume (Lilley et al., 1995). The strong linear relationship between Fe_{ex} and Mn_{ex} also argues against large-scale remobilization of either Fe or Mn even at sites with significant $Mn(II)_{aq}$ in pore fluids.

Sedimentary Mo abundance is a good indicator of sediment redox status: under oxic conditions Mo is scavenged by Mn oxides (Shimmield and Price, 1986); under suboxic conditions that lead to Mn dissolution, Mo is remobilized (Chaillou et al., 2002; McManus et al., 2002; Shimmield and Price, 1986); under reducing conditions Mo forms strong associations with sulphide

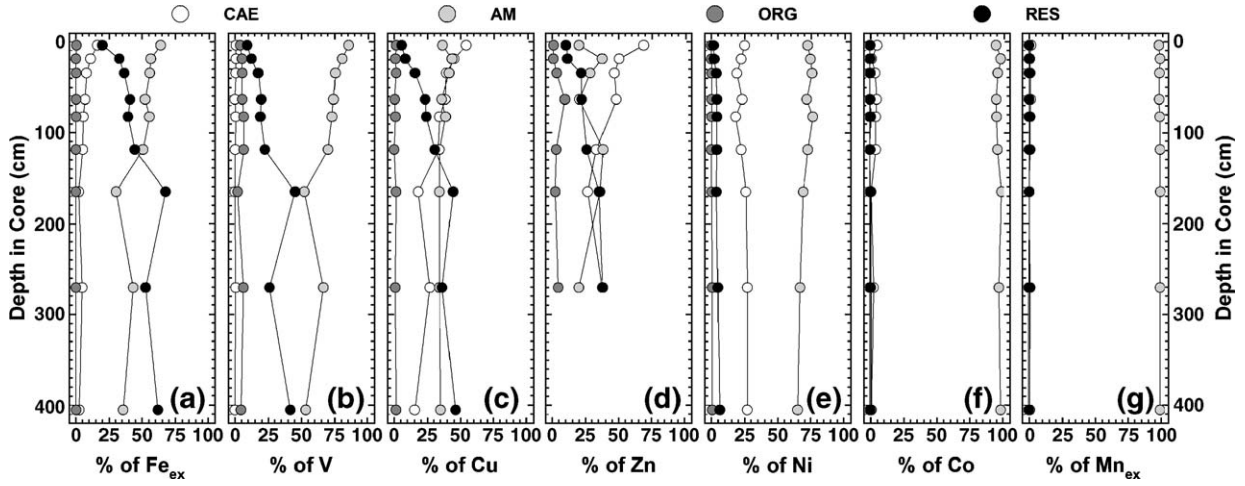

Fig. 5. Down-core speciation of transition metals as determined by a sequential extraction of 0.36 Ma site sediments. CAE = carbonate, adsorbed and exchangeable. AM = amorphous Fe oxyhydroxides and Mn oxides. ORG = organic. RES = residual, including crystalline Fe oxyhydroxides. (a) Fe_{ex}; (b) V; (c) Cu; (d) Zn; (e) Ni; (f) Co; and (g) Mn_{ex}.

species (Vorlicek et al., 2004). The Mo/Mn_{ex} ratios in the EXCO sediments are 0.0015 ± 0.0005 (1σ, $n=15$), 0.0007 ± 0.0002 (1σ, $n=19$) and 0.0044 ± 0.0021 (1σ, $n=7$) at the 0.36, 1.9 and 4.6 Ma sites respectively. In comparison, a fully oxic sediment core from the Pacific Ocean displayed a range in Mo/Mn of 0.0006–0.0019, with a mean of 0.0015 ± 0.0003 (Core 163–9; Shimmield and Price, 1986). The Mo/Mn_{ex} for the 0.36 Ma site are therefore consistent with dominantly oxic conditions, while the slightly lower values at the 1.9 Ma site suggest some Mo loss due to suboxic Mn cycling. The limited number of high values at the 4.6 Ma site are consistent with minor Mo uptake during early sulphide diagenesis (Vorlicek et al., 2004).

In summary, these data indicate dominantly oxic conditions in young near-axis sediments, changing to suboxic conditions across the ridge flank, where the constancy of the solid-phase Fe_{ex}/Mn_{ex} ratio and Mo/Mn_{ex} ratio at all sites argues against significant remobilization of hydrothermal Fe or Mn during diagenesis.

5.2. Sedimentation patterns across the EXCO study area

The contributions of the carbonate, detrital, and hydrothermal phases to the bulk sediment composition at the 0.36, 1.9 and 4.6 Ma sites are presented in Table 4. The sum of the components are approximately equal to 100 wt.% at all sites (100 ± 2 wt.%, 98 ± 3 wt.% and 101 ± 2 wt.%, respectively), demonstrating that the EXCO sediments are dominated by inputs from these sources, and supporting the choice of phase tracers and end-member compositions. In particular, Ti was chosen as the detrital phase tracer as the results clearly demonstrate that a significant proportion of sedimentary Al resides in the adsorbed or exchangeable fraction (Fig. 3), consistent with the hypothesis that scavenged Al makes a significant contribution to these sediments (cf. Dymond et al., 1997; Murray and Leinen, 1996; Murray et al., 1993).

In all cores, the relative importance of the sediment sources decreases in the following order: carbonate > hydrothermal > detrital. The contribution of carbonate to the sediments increases with increasing distance from the ridge axis, where the carbonate content is lowest at the 0.36 Ma site (64–95 wt.%) and highest at the 4.6 Ma sites (86–100 wt.%). A general up-core increase is also apparent at both the 0.36 and 1.9 Ma sites. The contribution of hydrothermal plume fall-out shows the opposite trend, with the highest hydrothermal component at the 0.36 Ma site (8–34 wt.%), lowest at the 4.6 Ma site (1–9 wt.%), and a general up-core decrease at the 0.36 and 1.9 Ma sites.

The distribution of detrital material is distinct from that of either the carbonate or hydrothermal components, where the detrital content at the 1.9 Ma site (0.4–1.0 wt.%) is lower than that at either the 0.36 Ma (0.7–8.5 wt.%) or 4.6 Ma (0.9–3.1 wt.%) sites. This pattern reflects the proximity of each site to local sources of basaltic debris. At the 0.36 Ma site, the detrital contribution is relatively low and constant in surface sediments (0–80 cmbsf; ~1 wt.%) and then increases with depth due to the increase in basalt input with

increasing proximity to the ridge axis. The comparatively high detrital component at the 4.6 Ma site is due to a continuous input of basaltic debris from exposed basement on the summit and flanks of the two large seamounts located in close proximity to the northeast and southwest (Fig. 1c).

5.2.1. Bulk sediment accumulation rates and hydrogenous metal inputs

A sediment accumulation rate (SAR) of 0.9–1.2 cm/ka in the near-axis region (0.36 Ma site) was estimated from those cores that reached basement (assuming linear sedimentation over time and no loss of core-top material), in excellent agreement with the ~1 cm/ka determined from seismic and echo-sounding surveys (Hauschild et al., 2003).

The relatively high SAR at the 0.36 Ma site precludes significant hydrogenous input. However in slowly accumulating sediments (SAR ~0.1 cm/ka), additional hydrogenous enrichment of trace metals can occur through continued scavenging from the overlying seawater (Bender et al., 1971; Marchig and Gundlach, 1982). Thus, if the bulk sedimentation rate decreases significantly across the ridge flanks (Hauschild et al., 2003), the hydrogenous contribution to the EXCO sediments will become important.

Ni and Co are considered sensitive indicators of hydrogenous input (Dymond, 1981). Although some scatter is evident in the Ni/Fe_{ex} and Co/Fe_{ex} ratios at the 0.36 Ma site (Fig. 4e and f), the relatively constant down-core distributions of Ni/Fe_{ex} and Co/Fe_{ex} (Fig. 6a and d) are consistent with a purely hydrothermal source for these elements. At the 1.9 Ma site, a significant up-core increase in Co/Fe_{ex}, and to a lesser extent in Ni/Fe_{ex}, is observed, where the majority of this increase occurs over the upper 100–150 cmbsf of the cores (Fig. 6b and e). At the 4.6 Ma site both Co/Fe_{ex} and Ni/Fe_{ex} are markedly higher than at either of the two younger sites (Fig. 6c and f). This clear increase in the Co/Fe_{ex} and Ni/Fe_{ex} ratios across the ridge flank is consistent with an additional hydrogenous enrichment of these elements that becomes of increasing importance as the ocean crust and overlying sediment moves off-axis.

These results indicate that in the near-axis region to the east of the SEPR bulk SARs are relatively high (~1 cm/ka), before decreasing rapidly to much lower values (~0.1–0.2 cm/ka) across the eastern ridge flank. This general pattern of sedimentation is in good agreement with that described by Hauschild et al. (2003), where these authors estimated that high sedimentation rates extended to crust aged 2 Ma (150 km from axis). However, that hydrogenous enrichment is apparent at depth (~100–150 cmbsf) within sediments at the 1.9 Ma site indicates that the decrease in SAR occurs somewhat before this point (within 142.5 km from axis), most likely between crust aged 0.4 and 1.5 Ma (between 30.0 and 112.5 km from axis).

5.2.2. Calcite dissolution across the eastern ridge flank

The asymmetry of sedimentation across the SEPR, with a relatively constant accumulation rate of ~1 cm/ka extending to 7 Ma on the western flank, and a rapid decrease in sedimentation rate across the eastern flank, has been attributed to the generation of sediment particles at the ridge axis and the west-ward transport of this material by prevailing ocean currents (Hauschild et al., 2003). This is consistent with the rapid decrease in the contribution of hydrothermal plume precipitates to east flank sediments with increasing distance from the ridge axis. Nonetheless, the asymmetric subsidence trend (Hauschild et al., 2003) suggests that enhanced calcite dissolution on the deeper eastern flank is also a contributing factor. Hauschild et al. (2003) excluded this second factor based on consideration of the reported depth of the lysocline (3500 m; Berger et al., 1976). However, it is more appropriate to consider calcite preservation within the context of the calcite saturation horizon (e.g. Milliman et al., 1999), which occurs at ca. 3000–3200 m in this area, the depth range approximately bracketed by the 0.36 Ma and 1.9 Ma sites (see Table 1). The decrease in sedimentation rate between these sites may therefore result from the onset of significant calcite dissolution within this region.

The grain size distribution of sediments at the 0.36 Ma site is relatively constant throughout the core (Fig. 6g). Conversely, at the 1.9 Ma site, while the size distribution of sediments at the base of the core is directly comparable to that seen at the 0.36 Ma site, there is a marked decrease in the contribution of the smallest size fraction (0–125 μm) from ~70–75 wt.% to ~50–55 wt.% over the upper 150 cm, and this corresponds directly to the depth at which hydrogenous enrichment becomes significant (Fig. 6h). This decrease in the contribution from the small size fraction could result from either (i) winnowing of the sediment at the seafloor under the influence of topographically controlled bottom currents (Kennett, 1982); (ii) a decreased input of small particles; or (iii) the preferential dissolution of small and fragmented foraminifera due to a higher effective surface area (Frenz et al., 2005).

Sediment winnowing is considered an unlikely explanation as seismic records show that the sediment

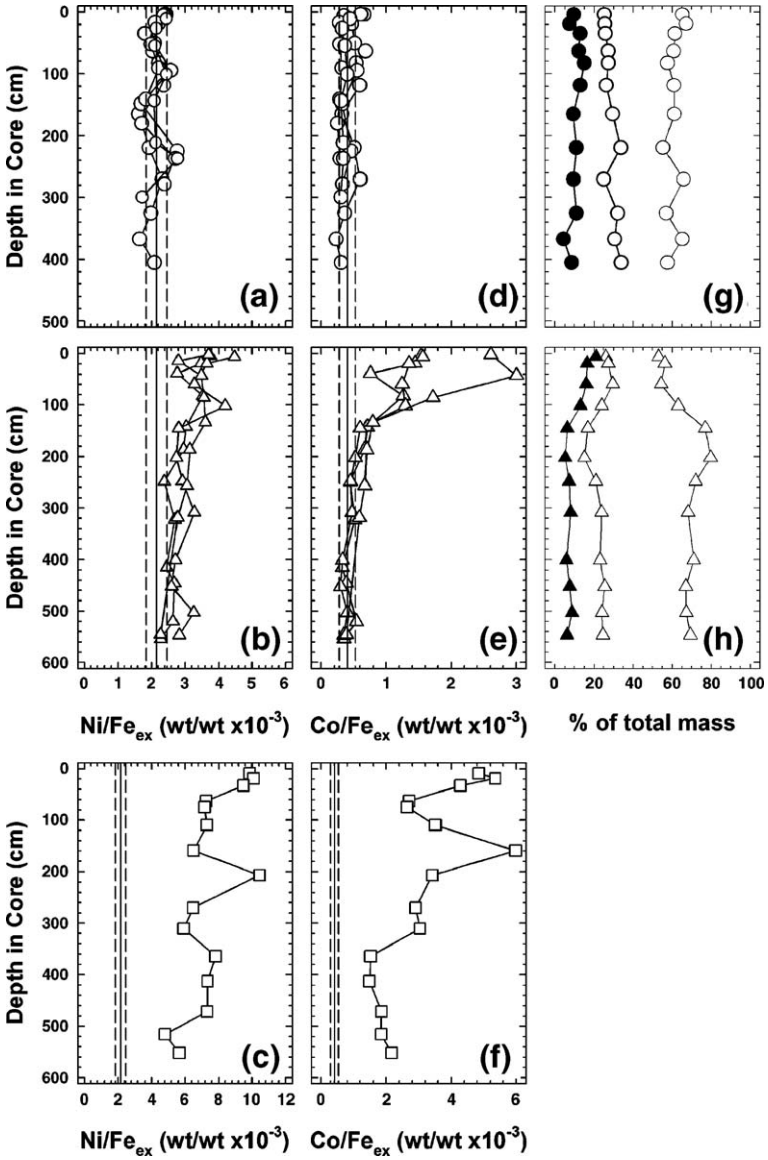

Fig. 6. (a–c) Ni/Fe$_{ex}$ at the 0.36, 1.9, and 4.6 Ma sites (d–e) Co/Fe$_{ex}$ at the 0.36, 1.9 and 4.6 Ma sites. Vertical solid lines indicate the mean ratio at the 0.36 Ma site, where dashed lines give $\pm 1\sigma$. Note that the 4.6 Ma data is presented on a different scale (×2) to that of the 0.36 and 1.9 Ma site data. (g, h) Grain size distribution at the 0.36 and 1.9 Ma sites (white=0–125 μm, gray=125–500 μm, black=>500 μm).

is draping basement rather than ponding (Hauschild et al., 2003). Hydrothermal plume particles reside in the small size fraction (1–10 μm, German and Sparks, 1993), and the up-core decrease in the plume input at the 1.9 Ma site (~8 wt.%) will contribute to the up-core decrease in the contribution of the small size fraction. However, this accounts for less than half of the total decrease (~20 wt.%), therefore carbonate dissolution must also be a significant factor in controlling the bulk sediment accumulation rates and thus the behaviour of Co and Ni across the ridge flank.

5.3. Plume particle alteration pathways

The predominant primary Fe oxyhydroxide mineral formed in hydrothermal plumes is poorly crystalline, fully hydrated, colloidal ferrihydrite, $Fe(OH)_3$ (Campbell, 1991; Feely et al., 1994). Particulate Mn is also enriched through the kinetic and bacterially mediated oxidation of hydrothermal Mn(II) (Cowen et al., 1990), and the dominant primary phase is most likely a poorly crystalline 10 Å manganate such as buserite (Glasby, 2006; Tebo et al., 2004). On delivery to the sediment

column, these plume particulates are subject to diagenesis, where the most important factor controlling the mode of alteration is the sedimentary redox status.

The geochemical evidence indicates that the sediments at the 0.36 Ma site are dominantly oxic (see Section 5.1). Under oxic conditions, ferrihydrite alteration is dominated by dehydration and transformation to more structurally ordered phases, and proceeds via two competing mechanisms, where conditions favouring the formation of goethite disfavour the formation of haematite and vice versa (Schwertmann and Murad, 1983; Schwertmann et al., 2004). Goethite (α-FeOOH) formation involves ferrihydrite dissolution followed by nucleation and precipitation (Schwertmann and Murad, 1983; Schwertmann et al., 2004). Haematite (α-Fe_2O_3) formation is less well understood and two possible mechanisms have been proposed: either internal atomic rearrangement of ferrihydrite combined with gradual complete dehydration (Towe and Bradley, 1967), or dissolution followed by adsorption of monomeric units at the ferrihydrite surface and subsequent dehydration to form oxo-bonds (Schwertmann et al., 2004). Hydrothermal Mn oxides may also undergo cycles of dissolution and re-precipitation to form more crystalline phases (e.g. Glasby, 2006).

Fe oxyhydroxides can also react with silica to form nontronite, a smectite type clay mineral (Cole, 1985; Heath and Dymond, 1977; Varnavas, 1988). However, the diagenetic formation of nontronite at low temperatures requires reducing conditions in the sediment column (the presence of porewater $Fe(II)_{(aq)}$; Harder, 1976), therefore this transformation pathway should be of minor importance in the EXCO sediments.

XRD analysis of the RES fraction of 0.36 Ma site sediments demonstrated that the dominant Fe oxyhydroxide alteration product in the EXCO sediments is goethite (Fig. 2b). While minor haematite was identified under the light microscope, it was not seen in the XRD patterns, confirming that the abundance of haematite in the EXCO sediments is low in comparison to that of goethite (<1% of the total crystalline Fe oxyhydroxide). A clay mineral was identified in some of the XRD patterns, which may indicate minor diagenetic formation of nontronite. However, the clay peaks are either weak or absent except in those samples with a comparatively high detrital input (E12#9 and E12#12). Furthermore, sample E12#7, where the hydrothermal plume input is at a maximum, shows no evidence for the presence of a clay mineral. Basaltic fragments showing evidence of alteration were recovered from the base of core E12 (Dunk, 2004), where Fe-rich celadonite is the dominant clay mineral in the EXCO basalt alteration assemblage (Schramm et al., 2005). This suggests that the clay mineral identified in the XRD patterns most likely results from the presence of altered basalt.

The lack of significant nontronite formation is in contrast to the alteration observed to the north of the EXCO study area where Fe oxyhydroxides show alteration to both goethite and smectite (Heath and Dymond, 1977; Varnavas, 1988). It has been suggested that nontronite formation is inhibited in regions of carbonate accumulation (Cole, 1985). However, the sediments at the Wilkes Fracture Zone (9°S), where formation of smectite clays is observed, have high carbonate contents of 60–87 wt.% (Varnavas, 1988), similar to the 64–95 wt.% observed in the near-axis region of the EXCO study area. Nevertheless, there are two distinct geochemical differences between these sites, firstly the redox status of the sediments, and secondly the availability of Si for reaction. There is only a weak correlation between sedimentary Fe and Mn in the Wilkes Fracture Zone sediments, indicating post depositional separation of these elements under reducing conditions (Varnavas, 1988). Furthermore, extensive volcanic ash deposits and a significant input of biogenic silica to the Wilkes Fracture Zone sediments results in a total SiO_2 content ranging from 15 to 34 wt.% (Varnavas, 1988). In comparison, the SiO_2 content of the sediments at the 0.36 Ma site is low, ranging from 1.9 to 7.1 wt.%, of which less than 0.7 wt.% can be attributed to biogenic silica (Dunk, 2004). The lack of significant nontronite formation in the EXCO sediments therefore reflects both the dominantly oxic conditions during diagenesis and the lack of Si available for reaction.

The dominant formation of goethite over haematite is consistent with the alteration observed in other oxic metalliferous deep-sea deposits, including carbonate-rich ridge flank sediments to the west of the SEPR at DSDP site 597 (Kastner, 1986), metalliferous muds forming the top stratum of a massive sulphide deposit at 18°S on the EPR (Dill et al., 1994), and within the carbonate cap of a massive sulphide deposit in the TAG hydrothermal field on the Mid-Atlantic Ridge (Severmann et al., 2006).

Ferrihydrite alteration in laboratory experiments has shown a clear product dependence on both reaction pH and temperature, with maximum haematite formation over the pH range 6–9, although the proportion of haematite formed decreases from ~75% of the total crystalline Fe oxyhydroxide at 25 °C to ~15% at 4 °C

(Schwertmann and Murad, 1983; Schwertmann et al., 2004). This maximum in haematite formation coincides with the $pH_{z.p.c.}$ (pH of zero point of charge) of ferrihydrite at pH 7.5–7.8 (Dzombak and Morel, 1990; Farley et al., 1985), and therefore the ferrihydrite solubility minimum, and has been attributed to either minimum goethite formation via dissolution and/or the maximum presence of ferrihydrite available for re-adsorption of dissolved monomers (Schwertmann and Murad, 1983; Schwertmann et al., 2004).

In the EXCO sediments the pH of the extracted interstitial porewaters (7.6–7.8, Mike Mottl, personal communication) coincides directly with the $pH_{p.z.c.}$ of ferrihydrite, and temperatures range from 1.8 °C at the sediment–seawater interface to ~3 °C at the sediment–basement interface (Villinger et al., 2002; Dunk, 2004). Under comparable conditions in the laboratory, haematite comprised ~15% of total crystalline Fe oxyhydroxide (Schwertmann et al., 2004). The lack of significant haematite formation (<1%) therefore suggests that either the formation of haematite is retarded and/or the formation of goethite is promoted. Furthermore, the general dominance of goethite in deep-sea metalliferous sediments suggests that the main alteration pathway is via dissolution followed by nucleation and precipitation. This mechanism could also explain the formation of discrete (as opposed to admixed) masses of secondary Fe oxyhydroxides and Mn oxides that were observed in the EXCO sediments. In contrast, the combined ferromanganese phases (mixed colloidal aggregates, infilling of foraminifera tests and micronodules) most likely formed through the direct transformation of amorphous Fe oxyhydroxides and Mn oxides in close physical association (i.e. coagulation of colloidal aggregates), resulting in an intimate association of hydrous manganates and amorphous Fe oxyhydroxides such as ferrihydrite (Halbach et al., 1981).

5.3.1. The extent and rate of Fe oxyhydroxide alteration

The extent and rate of plume particle alteration has been investigated through examination of the sequential extraction data from the 0.36 Ma site sediments (Fig. 5). In addition to amorphous Fe oxyhydroxides, all Mn oxides, including ferromanganese Mn, are extracted in the AM fraction (Fig. 5g), therefore no further information can be obtained regarding Mn alteration. However, the Fe oxyhydroxides are partitioned between the CAE, AM, and RES phases (Fig. 5a). The Fe_{CAE} is inferred to represent colloidal ferrihydrite, the most reactive portion of amorphous Fe in the sediments. Total amorphous Fe is therefore equal to the sum of the CAE and AM fractions ($Fe_{amorphous} = Fe_{(CAE+AM)}$). The high proportion of Fe in the RES fraction confirms that a significant proportion of the plume-derived Fe has been transformed to more crystalline phases, and based on the XRD patterns obtained (Fig. 2) it is assumed that this fraction (corrected for the detrital contribution) approximates to goethite Fe ($Fe_{goethite} = Fe_{RESex}$).

Two related parameters are routinely used in the literature to measure the extent of Fe oxyhydroxide transformation; the fraction (F) of total plume Fe remaining amorphous (e.g. Schwertmann and Murad, 1983; Eq. (7)) and the ratio (T) of goethite Fe to X-ray amorphous Fe (e.g. Kastner, 1986; Eq. (8)):

$$F = Fe_{amorphous}/Fe_{plume} = Fe_{(CAE+AM)}/Fe_{ex} \quad (7)$$

$$T = Fe_{goethite}/Fe_{amorphous} = Fe_{RESex}/Fe_{(CAE+AM)} \quad (8)$$

Thus F decreases and T increases with increasing extent of alteration, and these parameters can be readily inter-converted ($F = 1/(1+T)$). Here we favour the use of F, and calculated values for the 0.36 Ma site sediments are presented in Table 5. These young near-axis sediments give an F range of 0.3 to 0.8, where F shows a general decrease with depth in core,

Table 5
Extent of Fe alteration and associated V fractionation

Sample I.D.	Age (ka)	Fe_{plume} (mg/g)	$Fe_{amorphous}$ (mg/g)	$Fe_{goethite}$ (mg/g)	F	$(V/Fe)_{plume}$ (wt/wt)	$(V/Fe)_{amorphous}$ (wt/wt)	$(V/Fe)_{goethite}$ (wt/wt)
E12#1	3	28.8	23.0	5.7	0.80	0.0024	0.0026	0.0011
E12#2	16	51.3	34.5	16.7	0.67	0.0025	0.0030	0.0010
E12#3	29	39.1	24.8	14.2	0.63	0.0022	0.0027	0.0011
E12#4	53	32.5	19.2	13.3	0.59	0.0023	0.0029	0.0011
E12#5	69	31.4	19.1	12.3	0.61	0.0022	0.0027	0.0011
E12#6	99	32.4	18.0	14.3	0.56	0.0024	0.0030	0.0012
E12#7	138	119.1	38.5	80.4	0.32	0.0031	0.0050	0.0021
E12#9	226	40.2	19.2	20.9	0.48	0.0030	0.0043	0.0015
E12#12	339	59.5	22.7	36.6	0.38	0.0030	0.0042	0.0021

with a significant minimum in the most hydrothermal layer at 165 cmbsf (Table 5). In older (up to 24 Ma) more altered sediments from DSDP site 597 to the west of the SEPR at ~18°S, lower F ratios of 0.1 to 0.4 are observed (Kastner, 1986), consistent with increasing alteration with time. A more detailed comparison to these sediments is inappropriate due to differences in the analytical methods employed in determining F.

Determining the in situ rate of Fe oxyhydroxide alteration is difficult due to the large range in Fe_{ex}, the uncertainty in the estimate of F derived from the sequential extraction data and the inherent complexity of natural systems. Nevertheless, the relative simplicity of the EXCO sedimentary system allows some preliminary observations to be made. The most altered Fe oxyhydroxides occur at mid-depth in the sediment column, indicating that the extent of alteration is not a simple function of time, i.e. the transformation rate does not appear to follow first-order kinetics. Furthermore, the most altered samples are located within the hydrothermal-rich horizon, which suggests that the transformation rate may have a pseudo second-order dependency on the Fe oxyhydroxide concentration.

If it is assumed that Fe oxyhydroxide alteration can be approximated by a single irreversible reaction from amorphous Fe to goethite with rate constant k, where for each sample the initial concentration of amorphous Fe is equal to the total plume Fe delivered to the sediment column (at time $t=0$, $Fe_{amorphous}=Fe_{ex}$), then simple linear relationships for both first and second-order reaction kinetics can be derived based on F.

Under first-order kinetic control, F is dependent on t and k:

$$F = \exp^{-kt} \tag{9}$$

Under second-order kinetic control, F is dependent on t, k and Fe_{ex}:

$$F = 1/(1 + k^{*}t^{*}Fe_{ex}) \tag{10}$$

Thus for first- and second-order control respectively, a plot of $-\ln F$ vs. t, or a plot of $(1-F)/F$ vs. $t^{*}Fe_{ex}$, would give a straight line with slope k. Both plots are shown in Fig. 7, where the value of t is the time since deposition calculated assuming a linear sediment accumulation rate (1.2 cm/ka) for core E12.

Although neither model shows a perfect fit to the data, model II (geometric mean) regressions of the data indicate a significantly better fit to the second-order model ($R=0.93$) as opposed to the first-order model ($R=0.77$), suggesting that the alteration of ferrihydrite to goethite in natural systems does not follow first-order kinetics and providing some evidence for higher order reaction kinetics in the EXCO sediments. This result is in contrast to laboratory experiments that show a first-order dependence on ferrihydrite (e.g. Schwertmann and Murad, 1983). The apparent second-order dependency may result from the profound difference in the physical environment of alteration between Fe oxyhydroxide in suspension and Fe oxyhydroxide in the sediment column; where the physical properties of the sediment that define the alteration environment (e.g. porosity) are in turn dependent on the Fe oxyhydroxide content of the sediment. For example, a strong inverse relationship is observed between F and

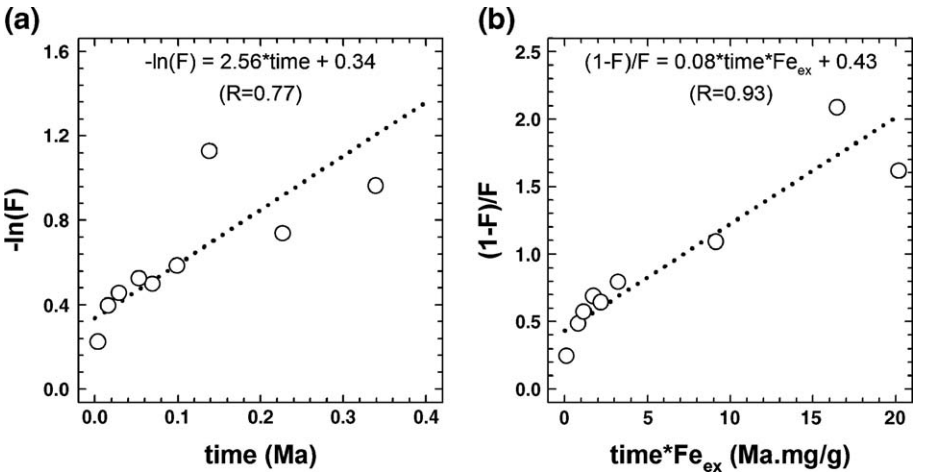

Fig. 7. Investigation of Fe alteration reaction kinetics. (a) first order control: $-\ln(F)$ vs. time, slope k; (b) second order control: $(1-F)/F$ vs. time * Fe_{ex}, slope k. F is the fraction of total plume Fe remaining amorphous. Lines give type II (geometric mean) regressions of the data.

sediment porosity, with a type II (geometric mean) linear regression giving $R=-0.86$.

Irrespective of the reaction order, the rate of plume-derived ferrihydrite transformation is extremely slow with respect to the alteration of synthetic ferrihydrite, with a time to half conversion (THC) in the natural system on the order of ~100 ka in comparison to a THC on the order of ~1000 days in laboratory experiments at comparable pH and temperature (Schwertmann et al., 2004).

One possible mechanism that could explain both the retardation of the ferrihydrite transformation rate, and the lack of haematite formation at circumneutral pH, is a purely inorganic process, whereby adsorbed species scavenged from seawater during plume dispersal inhibit the formation of haematite (preventing either the structural rearrangement of ferrihydrite to haematite, or blocking the adsorption of dissolved monomers to the ferrihydrite surface). Previous studies have shown that the presence of impurities (co-precipitates and/or adsorbed species) act as inhibitors of transformation of poorly ordered ferrihydrite, stabilizing this highly reactive phase in the sediment column (see review by Jambor and Dutrizac, 1998 and references therein).

More recently, studies on bacteriogenic ferrihydrite have demonstrated complete inhibition of haematite formation, which is attributed to complexation between the ferrihydrite and microbial surface functional groups (Kennedy et al., 2004). Microbial communities, including Mn-oxidizing bacteria, colonize particulate Fe oxyhydroxides and Mn oxides associated with vent plumes (Cowen and Silver, 1984; Mandernack and Tebo, 1993), and may therefore play a role in haematite retardation.

Alternatively the alteration of Fe oxyhydroxides could be driven by bacterially mediated dissimilatory Fe reduction, which would result in the dissolution of bioavailable amorphous Fe and therefore promote the formation of goethite. However, this process occurs under suboxic conditions and leads to the production of $Fe(II)_{aq}$ (Glasauer et al., 2003), consequently this mechanism might also be expected to lead to the separation of solid phase Fe and Mn in the sediment column (e.g. Froelich et al., 1979) and promote the formation of nontronite (e.g. Harder, 1976). Although the EXCO sediments at the 0.36 Ma site are a dominantly oxic environment, dissimilatory Fe reduction could feasibly occur in reducing micro-environments within the sediment column. Significant numbers of Fe(III)-reducers have been inferred to exist in microenvironments within the oxic (zero Fe $(II)_{aq}$, zero $Mn(II)_{aq}$) carbonate-rich metalliferous sediments from the TAG hydrothermal field on the Mid-Atlantic Ridge, where goethite is also the dominant Fe oxyhydroxide alteration product (Severmann et al., 2006).

5.4. Transition metal phase associations and behaviour during diagenesis

The plume particle flux is the major source of transition metals to the EXCO sediments, with a secondary hydrogenous input becoming of increasing importance with increasing distance from the ridge axis.

The scavenging properties of hydrous Fe and Mn phases differ due to different surface charge characteristics, described by the $pH_{z.p.c.}$ of the phase in question (Murray, 1979). Fe oxyhydroxides have a $pH_{z.p.c.}$ of 7–8, whereas hydrous manganates have a $pH_{z.p.c.}$ of 2–3. Therefore under seawater conditions, Fe oxyhydroxides act as efficient scavengers of neutral and negatively charged species such as the oxyanions and divalent transition metal (TM) carbonate or sulphate complexes (e.g. HVO_4^{2-}, $TMCO_3^0$, $TMSO_4^0$), whereas Mn oxides hold a high density of negative charge and act as an efficient sink of cationic species such as the free divalent transition metal ions and the hydroxyl and chloride complexes (e.g. TM^{2+}, $TMOH^+$, $TMCl^+$).

Secondary crystalline minerals generally have a lower surface area than the primary amorphous phase. The oxic alteration of Fe oxyhydroxides and Mn oxides may therefore lead to a reduction in the sorption capacity of the sediment and the release of sorbed elements to the solution phase. However, laboratory experiments have demonstrated that divalent transition metals can become incorporated into the goethite structure by isomorphous substitution for Fe^{3+} (Gerth, 1990). As the susceptibility of Fe oxyhydroxides to dissolution also decreases with increasing crystallinity, the alteration of plume precipitates may result in a relatively permanent sink for transition metals where goethite dissolution becomes a prerequisite for metal release.

The sedimentary speciation of the transition metals studied here (the oxyanion V, and divalent transition metals Cu, Zn, Ni, Co) showed a continuum between Fe and Mn type behaviour during alteration (Fig. 5), from which the dominant phase associations of these metals on delivery to the sediment, and the differential incorporation into goethite during alteration, can be deduced.

5.4.1. Vanadium

Although bottom water V concentrations are relatively constant throughout the worlds oceans at 1.8–1.9 μg/kg (35–37 nmol/kg; Collier, 1984; Jeandel et al., 1987), the V/Fe ratio of plume particles varies geographically, and shows a strong inverse correlation to bottom water PO_4^{3-} concentrations (Edmonds and German, 2004; Feely et al., 1998). This has been attributed to competitive scavenging, where vanadate does not compete as well as phosphate for the available sites on ferrihydrite particles, and has led to the suggestion that metalliferous sediments may record variations in the seawater concentration of P and V over time (Edmonds and German, 2004; Feely et al., 1998). Moreover, hydrothermal scavenging represents a significant removal mechanism in the geochemical cycling of V, accounting for approximately one-third of the riverine input (Morford and Emerson, 1999). However, both the magnitude of the hydrothermal V sink and the use of sedimentary V/Fe ratios as a tracer of past seawater composition are dependent on the preservation of the initial plume V/Fe input during diagenesis.

The present day plume V/Fe (wt/wt) elemental ratio in the EXCO study area is 0.0027±0.0005 (RIDGEFLUX, data from 13° to 16°S on the SEPR; Feely et al., 1996). The sedimentary V data are plotted against Fe_{ex} for all sites in Fig. 4b. A model II (geometric mean) linear regression of this data gives a V/Fe_{ex} ratio of 0.0031 ($R=0.99$), slightly higher than the mean V/Fe_{ex} of 0.0024 ±0.003 (1σ, $n=81$). Both estimates of the sedimentary V/Fe_{ex} ratio are within the range of the plume particulates, which confirms that the only significant source of V to the sediments is the hydrothermal input. A more detailed examination of the data shows a decrease in V/Fe_{ex} across the ridge flanks, from 0.0026±0.0003 (1σ, $n=34$) at the 0.36 Ma site, to 0.0023±0.003 (1σ, $n=32$) and 0.0022 ±0.0003 (1σ, $n=15$) at the 1.9 Ma and 4.6 Ma sites respectively, where the difference between the 0.36 Ma and the two older sites is significant at the 99.5% confidence level (Student's *t*-test). These data suggest complete retention of plume V in oxic near-axis sediments, with minor loss of V from the sediment column as conditions change to suboxic across the ridge flanks. This hypothesis is supported by the V distribution at the intermediate 1.9 Ma site, where core E20 (oxic) has a V/Fe_{ex} of 0.0024±0.0003 (1σ, $n=12$; not significantly different to the 0.36 Ma site), and cores E10 and E24 (suboxic) have a mean V/Fe_{ex} of 0.0022±0.0002 (1σ, $n=20$; equal to the 4.6 Ma site).

As expected from the known association between Fe oxyhydroxides and HVO_4^-, the down-core fractionation of V at the 0.36 Ma site is very similar to that of Fe_{ex} (Fig. 5a and b). However, $(V/Fe_{ex})_{RES}$ (considered here to be equal to (V/Fe) goethite) is low with respect to $(V/Fe_{ex})_{bulk}$, indicating that V is discriminated against during transformation of ferrihydrite to goethite (see Table 5). Furthermore, the high $(V/Fe)_{AM}$ indicates that the rejected V is retained in the sediment column through either strong surface complexation to the remaining ferrihydrite or via incorporation into ferromanganese phases. Similar results have been observed in hydrothermal sediments from the Lau Basin, where the relative proportion of V to Fe in the acid reducible fraction (directly comparable to the AM fraction) was significantly higher than that observed in the HCl soluble fraction (which includes crystalline Fe oxides) (Cronan and Hodkinson, 1997).

Here we present an estimate of the degree of V discrimination, based on the following assumptions: (i) plume Fe is delivered to the sediment with an initial $(V/Fe)_{plume}$ equal to $(V/Fe_{ex})_{bulk}$, where at time $t=0$ all Fe is in the amorphous fraction; (ii) goethite formation proceeds via a dissolved pool, where the distribution coefficient for V between goethite and the dissolved pool is constant and less than 1 ($D_V=(V/Fe)_{goethite}/(V/Fe)_{dissolved}<1$); (iii) all rejected V is incorporated into amorphous Fe phases; and (iv) that at time *t*, $(V/Fe)_{dissolved}$ is equal to $(V/Fe)_{amorphous}$, or $(V/Fe)_{(CAE+AM)}$. These assumptions allow us to consider this reaction as a simple Rayleigh crystallization, where $(V/Fe)_{dissolved}$, and therefore $(V/Fe)_{amorphous}$, at time *t* is given by:

$$(V/Fe)_{amorphous} = (V/Fe)^*_{plume} F^{(D_V-1)} \quad (11)$$

And applying mass balance, $(V/Fe)_{goethite}$ at time *t* is given by:

$$(V/Fe)_{geothite} = \left[(V/Fe)_{plume} - F^*(V/Fe)_{amorphous}\right] / (1-F) \quad (12)$$

where *F* is the fraction of Fe remaining amorphous (see Eq. (7)).

These equations were then solved for D_V, where the best-fit solution was obtained by minimizing the sum of the squares of the residual difference between the observed and theoretical (V/Fe) across all samples for (a) $(V/Fe)_{goethite}$, (b) $(V/Fe)_{amorphous}$ and $(V/Fe)_{dissolved}$, and (c) both parameters, giving an estimated D_V in the range of 0.45–0.59 (see Fig. 8).

The best fit for $(V/Fe)_{goethite}$ is obtained for the lower limit on D_V of 0.45. Although the $(V/Fe)_{dissolved}$ predicted by this model shows the same general trend as $(V/Fe)_{amorphous}$, and increases with decreasing *F* (increasing alteration), significant differences are

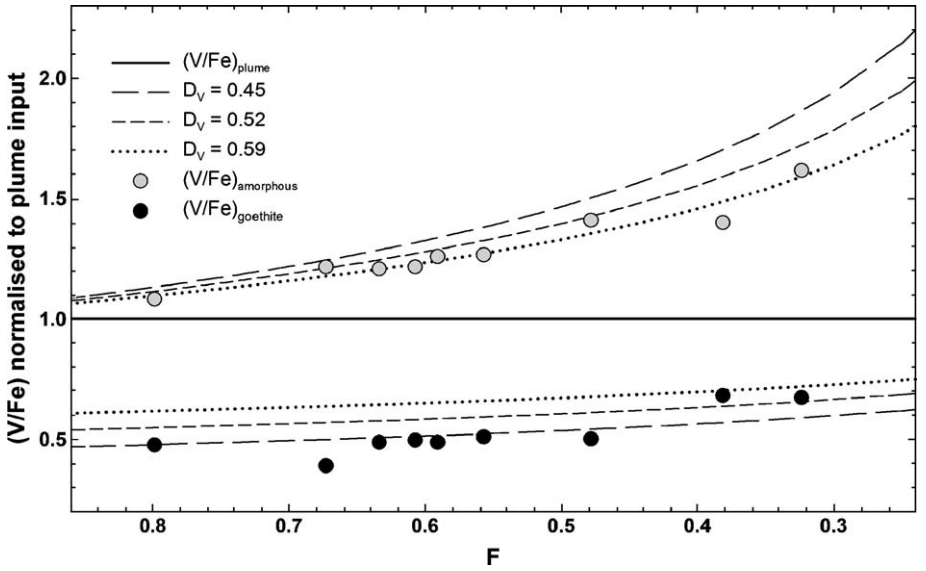

Fig. 8. Comparison of the observed (symbols) and predicted (lines) V/Fe ratios in goethite and amorphous Fe oxyhydroxide for a distribution coefficient (D_V) of 0.45–0.59. All ratios are normalized to a plume V/Fe of 1.

observed. Specifically, $(V/Fe)_{dissolved}$ is consistently greater than $(V/Fe)_{amorphous}$, and the difference between these parameters increases with increasing alteration (see Fig. 8). This discrepancy reflects assumption (iv) above, which carries the inherent supposition that the amorphous phase has a uniform (V/Fe) ratio. It is the external surfaces of the plume ferrihydrite that are available as sites of V retention, hence the $(V/Fe)_{amorphous}$ of external sites will be higher than both the internal and bulk $(V/Fe)_{amorphous}$. Furthermore, it is the external surfaces to which rejected V will re-adsorb. The fact that $(V/Fe)_{dissolved}$ is somewhat higher than the observed bulk $(V/Fe)_{amorphous}$, and that the discrepancy between these parameters increases with increasing alteration, is perhaps to be expected, and we consider the lower limit on D_V to be the best estimate. If it is assumed that V association with both ferrihydrite and goethite occurs through surface complexation, the estimated value of D_V suggests that the transformation of ferrihydrite to goethite results in a reduction in the number of surface adsorption sites by ~55%.

The bulk V/Fe_{ex} ratio in the EXCO sediments therefore largely reflects the plume input to this site over several Ma, though there is evidence for minor loss of V during suboxic diagenesis in the older EXCO sites. It is apparent from these data that there is potential for significant V loss during only mildly reducing conditions compromising the sedimentary V/Fe record (e.g. Schaller et al., 2000). As it is the amorphous Fe oxyhydroxide phases that are most susceptible to suboxic dissolution, the high susceptibility of these ridge flank sediments to V loss most likely reflects the enrichment of V within the amorphous Fe fraction during early oxic diagenesis. Nevertheless, application of the sedimentary V/Fe ratios as a proxy for past ocean PO_4^{3-} levels (e.g. Edmonds and German, 2004; Feely et al., 1998) has potential in fully oxic plume-derived sediments, such as those found in the near-axis region of the EXCO study site.

5.4.2. Copper and zinc

Cu and Zn are enriched in hydrothermal fluids with respect to seawater and are chalcophile elements that show a primary association with sulphide phases such as chalcopyrite and sphalerite that precipitate within the first few seconds following injection of the hydrothermal fluid into ambient bottom water (Feely et al., 1992). These sulphide minerals are subject to oxidative dissolution and differential sedimentation, which act to alter the composition of hydrothermal suspended matter and lead to a non-linear relationship between Cu or Zn and Fe in near-field plume particles (Feely et al., 1987, 1990b, 1992; Lilley et al., 1995; Trocine and Trefry, 1988). Conversely, in the far-field EXCO sediments (excluding the 4.6 Ma site where minor hydrogenous enrichment of Cu is observed), Cu and Zn display a constant linear relationship with Fe_{ex} (Fig. 4c and d; Cu/Fe_{ex} (wt/wt) $= 5.0 \times 10^{-3}$, Zn/Fe_{ex} (wt/wt) $= 1.9 \times 10^{-3}$), and a good agreement is observed with the hydrothermal end-member of Dymond (1981) (Cu/Fe (wt/wt) $= 4.2 \times 10^{-3}$, Zn/Fe (wt/wt) $= 1.9 \times 10^{-3}$). This implies a strong and regular association of these elements with

the hydrothermal plume material, suggesting that sulphides are not the primary Cu and Zn carrying phase, and that co-precipitation and sorption reactions with Fe oxyhydroxides and Mn oxides have a greater influence on particle chemistry within the neutrally buoyant plume.

The fractionation of Cu and Zn in the sequential extraction is consistent with an association with both Fe oxyhydroxides and Mn oxides (Fig. 5). The fraction of TM residing in the AM fraction is essentially constant down-core, and displays a stronger correlation to Mn_{AM} (Cu, $R=0.99$; Zn, $R=0.98$) than to Fe_{AM} (Cu, $R=0.91$, Zn, $R=0.94$). TM_{CAE} mirrors the down-core decrease in $Fe_{amorphous}$ (Cu, $R=0.92$, Zn, $R=0.91$), and TM_{RES} mirrors the down-core increase in Fe_{RESex} (Cu, $R=0.99$, Zn, $R=0.97$). We therefore infer that the AM fraction represents TM dominantly associated with Mn oxides, whereas the CAE fraction reflects the less strongly held TM absorbed to the ferrihydrite surface. The down-core decrease in TM_{CAE} and concomitant increase in TM_{RES} is consistent with incorporation of ferrihydrite-absorbed Cu and Zn into the goethite structure during alteration. The close agreement of the $(Cu/Fe_{ex})_{RES}$ and $Cu_{CAE}/Fe_{amorphous}$ ratios (3.6×10^{-3} and 3.4×10^{-3}, respectively) suggests that Cu is incorporated into goethite without discrimination. Although the $(Zn/Fe_{ex})_{RES}$ is slightly lower than the $Zn_{CAE}/Fe_{amorphous}$ ratio (1.2×10^{-3} and 2.0×10^{-3}), within the uncertainties of the Zn data these ratios cannot be considered significantly different and it would appear that Zn is also incorporated into the goethite structure with little or no discrimination.

In laboratory experiments, Savenko (2001) has shown a high efficiency of Zn and Cu co-precipitation with ferrihydrite, where the TM/Fe ratio in the precipitate was directly dependent on the TM/Fe ratio in the initial solution. The concentration of Cu and Zn in Pacific bottom waters are ca. ~200 ng/kg and ~600 ng/kg, respectively (Martin et al., 1989); thus, if these elements were scavenged from seawater, a Cu/Zn (wt/wt) ratio within the Fe oxyhydroxide fraction of ~0.3 would be expected. The observed ratio within the CAE fraction is significantly higher at 1.9 ± 0.2, which suggests that a proportion of the Cu is of hydrothermal origin. This is consistent with a study of Cu behaviour within plumes on the Mid Atlantic Ridge, where up to 43% of hydrothermally injected Cu resided within the dissolved fraction (operationally defined as <0.4 μm), and was inferred to represent dissolved Cu that has not been removed as sulphides and/or Cu associated with fine grained colloidal Fe oxyhydroxides (James and Elderfield, 1996).

The fractionation of Cu and Zn between Fe oxyhydroxide and Mn oxide phases within hydrogenetic Fe–Mn crusts has been shown to reflect the seawater speciation of these elements (Koschinsky and Hein, 2003). Approximately ~80% of seawater Cu occurs as neutral carbonate complexes (Byrne et al., 1988), and Cu is dominantly associated with Fe oxyhydroxides (64–85%), whereas ~85% of Zn occurs as cationic species (Stanley and Byrne, 1990), and Zn is dominantly associated with Mn oxides (61–83%) (Koschinsky and Hein, 2003). The observed fractionation of Cu in the EXCO sediments is very similar to that observed in hydrogenetic crusts, with ~60% of Cu associated with Fe oxyhydroxides. However, only ~30% of Zn in the EXCO sediments is associated with Mn oxides, therefore in contrast to the formation of hydrogenetic samples, the solid phase fractionation of Zn in the plume particulates does not reflect the aqueous speciation of Zn in the plume (which, given rapid dilution with seawater by a factor of 10^4–10^5 (Baker et al., 1995; Lupton, 1995), would be similar to seawater, thereby also promoting a dominant association with Mn oxides). Rather, the dominant association of both Cu and Zn with the Fe oxyhydroxides is most likely related to the rapid oxidation of Fe(II) to Fe(III) and concomitant formation of ferrihydrite within the first few seconds of plume rise, with respect to the slower oxidation kinetics of Mn(II) to Mn(IV) and the formation of Mn oxide phases; i.e. uptake of Zn and Cu occurs initially through scavenging of neutral TM complexes by abundant Fe oxyhydroxides, and it is the low comparative concentration of Mn oxides during the early stages of plume scavenging that results in the observed fractionation.

5.4.3. Nickel and cobalt

As discussed above (Section 5.2.1), Ni and Co both show evidence of hydrogenous enrichment in older sediments at the 1.9 and 4.6 Ma sites. Although some scatter is observed in the Ni/Fe_{ex} and Co/Fe_{ex} ratios at the 0.36 Ma site (Fig. 4e and f), significant hydrogenous enrichment is inconsistent with the relatively high sedimentation rates in this region. It would therefore appear that the Ni and Co content of hydrothermal plume material is somewhat variable.

The fractionation of Ni and Co in the sequential extraction is consistent with a dominant association with Mn oxides. Most of the Ni resides in the CAE and AM fractions (~25% and ~75%, respectively). Although Ni_{RES} is minor, a reasonable correlation is observed to Fe_{RESex} ($R=0.83$), giving an $(Ni/Fe_{ex})_{RES}$ (wt/wt) of ~0.1–0.2×10^{-3}. The distribution of Co is most similar to Mn, with 95–99% of total Co occurring within the

AM fraction (95–99%). The remainder of Co is found within the CAE fraction, with zero Co in the RES fraction (below detection limits). The low $(Ni/Fe_{ex})_{RES}$ with respect to $(Ni/Fe_{ex})_{bulk}$, and zero Co_{RES}, imply that either Ni and Co are rejected during alteration of ferrihydrite to goethite, or that these metals have a much stronger affinity for Mn oxides. If rejection were occurring, then progressive alteration should result in a concomitant increase in $(TM/Fe)_{amorphous}$, which is not seen in the data. The constancy of the down-core fractionation therefore indicates a dominant association with Mn oxides, where Ni_{RES} most likely represents Ni initially co-precipitated with ferrihydrite and incorporated into the goethite without discrimination. This sedimentary speciation of Co and Ni is consistent with that observed in manganese nodules, and indicate that cationic species account for greater than 90% of dissolved Ni and Co in seawater (Koschinsky and Hein, 2003).

6. Conclusions

The sediments in the EXCO study area are lithologically simple, and can be well described by a three component mixing model consisting of biogenic carbonate, hydrothermal plume precipitates, and locally sourced basaltic debris, where the relative importance of these components decreases in the following order: carbonate > hydrothermal > detrital. The accumulation rate of calcium carbonate in the EXCO sediments decreases with increasing distance from the spreading axis, primarily due to the decreasing preservation of calcite as the seafloor subsides and moves beneath the calcite saturation depth. The input of hydrothermal plume precipitates decreases with increasing distance from the axial source. Additional minor mineral phases, identified by X-ray diffraction and energy dispersive X-ray analysis of SEM images, are opaline silica, barite, and a clay material. The low refractory organic carbon content, and the close agreement of the Fe_{ex}/Mn_{ex} ratio, the low porewater Mn content and the relatively constant Mo/Mn ratio all indicate minimal redox disturbance during diagenesis.

The early diagenetic alteration of plume material deposited in the EXCO sediments is dominated by the transformation of metal oxyhydroxides towards structures of higher crystalline orders (i.e. dehydration). The alteration of Fe oxyhydroxides in the EXCO sediments is dominated by transformation of ferrihydrite to goethite, and the formation of haematite and nontronite are of minor significance in comparison to this reaction pathway. The time to half conversion for ferrihydrite alteration is on the order of ~100 ka. The almost exclusive formation of goethite and slow reaction rates are consistent with strong retardation of ferrihydrite alteration to haematite via structural rearrangement, and indicate that the dominant alteration pathway occurs via dissolution followed by nucleation and precipitation. Both the presence of adsorbed and/or co-precipitated oxyanion and divalent transition metal species and or the presence of bacteria may be responsible for the stabilization of ferrihydrite in deep-sea sediments.

V is delivered to the sediment column in association with plume-derived Fe oxyhydroxides. V is strongly discriminated against during the oxic alteration of ferrihydrite to goethite, where the distribution coefficient between goethite and the dissolved pool ($D_V = (V/Fe)_{goethite}/(V/Fe)_{dissolved}$) is ~0.45. The rejected V is retained in the sediment column through complexation with either the remaining ferrihydrite or the remaining ferromanganese phases. Under oxic conditions in the near-axis region, plume particle V/Fe ratios are preserved in the sediment column, suggesting that these sediments may provide a valuable record of past ocean V/P ratios. However, the concentration of V in the amorphous fraction during early oxic diagenesis makes this element highly susceptible to remobilization under suboxic conditions, and there is evidence for V loss from ridge flank sediments.

The divalent transition metals Cu, Zn, Ni and Co are delivered to the sediment in association with hydrothermal Fe oxyhydroxides and Mn oxides, where the concentration in the plume material decreases in the following order: Cu > Zn ≈ Ni > Co. An additional hydrogenous input of Co and Ni was apparent in surficial sediments at the 1.9 Ma site and at the 4.6 Ma site. In hydrothermal sediments, the accumulation of Co is a more sensitive indicator of additional hydrogenous enrichment than Ni. Approximately 60–70% of Cu and Zn are associated with Fe oxyhydroxides, with the remainder associated with Mn oxides. The Fe-associated Cu and Zn are initially adsorbed to the ferrihydrite surface and are incorporated without discrimination into the lattice structure of goethite during alteration. Approximately 10% of Ni is associated with Fe oxyhydroxides, with the remaining 90% associated with Mn oxides. The Fe-associated Ni most likely represents Ni co-precipitated as an Ni–Fe ferrihydrite and incorporated into the goethite structure without discrimination during alteration. Approximately 95–99% of excess Co is associated with Mn oxides, where the remainder is adsorbed to the sediment. The transformation of hydrothermal plume material under oxic conditions therefore represents a relatively permanent

sink (where goethite dissolution becomes a prerequisite for metal release) for a maximum of ~70% of the plume-derived Cu and Zn, 45% of V, 10% of Ni, and 0% of Co.

Acknowledgements

We thank the chief scientist of EXCOII/2, Colin Devey, the shipboard scientific party, and the Captain and crew of the *R/V Sonne*. Particular thanks are extended to Geoff Wheat and Mike Mottl for both the use of porewater data and helpful discussions regarding this manuscript. Darryl Green (ICP–AES), Sarah Glynn (microscopy), and Ross Williams (XRD) provided invaluable laboratory assistance at the NOC. This work was supported by NERC through grant GR3/11984 to R. A. Mills and W. J. Jenkins and studentship GT/04/99/ES/256 to R. M. Dunk. We also thank G.P. Glasby and an anonymous reviewer for their helpful comments on this manuscript.

References

Baker, E.T., German, C.R., Elderfield, H., 1995. Hydrothermal plumes over spreading-center axes: global distributions and geological inferences. In: Humphris, S.E., Zierenberg, A., Mullineaux, L.S., Thomson, R.E. (Eds.), Seafloor Hydrothermal Systems. Geophys. Monogr., Am. Geophys. Union, vol. 91, pp. 47–71.

Bayon, G., German, C.R., Boella, R.M., Milton, J.A., Taylor, R.N., Nesbitt, R.W., 2002. An improved method for extracting marine sediment fractions and its application to Sr and Nd isotopic analysis. Chem. Geol. 187, 179–199.

Bender, M.L., Broecker, W., Gornitz, V., Middel, U., Kay, R., Sunn, S. S., Biscaye, P., 1971. Geochemistry of three cores from the East Pacific Rise. Earth Planet. Sci. Lett. 12, 425–433.

Berger, W.H., Adelseck, C.G., Mayer, L.A., 1976. Distribution of carbonate in surface sediments of the Pacific Ocean. J. Geophys. Res. 81, 2617–2627.

Bostrum, K., Peterson, M.N.A., Joensuu, O., Fisher, D.E., 1969. Aluminium poor ferromanganoan sediments on active oceanic ridges. J. Geophys. Res. 74, 3262.

Byrne, R.H., Kump, L.R., Cantrell, K.J., 1988. The influence of temperature and pH on trace metal speciation in seawater. Mar. Chem. 25, 163–181.

Campbell, A.C., 1991. Mineralogy and chemistry of marine particles by synchrotron X-ray spectrometry, Mossbauer spectrometry, and plasma–mass spectrometry. In: Hurd, D.C., Spencer, D.W. (Eds.), Geophys. Monogr., Am. Geophys. Union, vol. 63, pp. 375–390.

Chaillou, G., Anschutz, P., Lavaux, G., Schafer, J., Blanc, G., 2002. The distribution of Mo, U, and Cd in relation to major redox species in muddy sediments of the Bay of Biscay. Mar. Chem. 80, 41–59.

Chester, R., Hughes, M.J., 1967. A chemical technique for the separation of ferro-manganese minerals, carbonate minerals and adsorbed trace elements from pelagic sediments. Chem. Geol. 2, 249–262.

Cole, T.G., 1985. Composition, oxygen isotope geochemistry, and origin of smectite in the metalliferous sediments of the Bauer Deep, southeast Pacific. Geochim. Cosmochim. Acta 49, 221–235.

Collier, R.W., 1984. Particulate and dissolved vanadium in the North Pacific Ocean. Nature 309, 441–444.

Cowen, J.P., Silver, M.W., 1984. The association of iron and manganese with bacteria on marine macroparticulate material. Science 224, 1340–1342.

Cowen, J.P., Massoth, G.J., Feely, R.A., 1990. Scavenging rates of dissolved manganese in a hydrothermal vent plume. Deep-Sea Res. 37, 1619–1637.

Cronan, D.S., Hodkinson, R.A., 1997. Geochemistry of hydrothermal sediments from ODP sites 834 and 835 in the Lau Basin, southwest Pacific. Mar. Geol. 141, 237–268.

Dill, H.G., Siegfanz, G., Marchig, V., 1994. Mineralogy and chemistry of metalliferous muds forming the top-stratum of a massive sulfide–metalliferous sediment sequence from East Pacific Rise 18°S: its origin and implications concerning the formation of ochrous sediments in Cyprus-type deposits. Mar. Georesour. Geotechnol. 12, 159–180.

Dunk, R.M., 2004. A geochemical study of ridge flank sediments on the East Pacific Rise and the development of uranium as a tracer of low temperature hydrothermal circulation. PhD thesis, University of Southampton, Southampton, UK. 310 pp.

Dymond, J., 1981. Geochemistry of Nazca plate surface sediments: an evaluation of hydrothermal, biogenic, detrital, and hydrogenous sources. Geol. Soc. Am. Mem. 154, 133–172.

Dymond, J., Roth, S., 1988. Plume dispersed hydrothermal particles: a time-series record of settling flux from the Endeavour Ridge using moored sensors. Geochim. Cosmochim. Acta 2, 2525–2536.

Dymond, J., Corliss, J.B., Stillinger, R., 1976. Chemical composition and metal accumulation rates of metalliferous sediments from sites 319, 320B and 321. In: Yeats, R.S., Hart, S.R., et al. (Eds.), Initial Reports of the Deep Sea Drilling Project 34. US Government Printin Office, Washington, pp. 575–588.

Dymond, J.E., Collier, R., McManus, J., Honjo, S., Manganini, S., 1997. Can the aluminium and titanium contents of ocean sediments be used to determine the paleoproductivity of the oceans? Paleoceanography 12, 586–593.

Dzombak, A.D., Morel, F.M.M., 1990. Surface Complex Modelling. Hydrous Ferric Oxide. J. Wiley, Germany. 393 pp.

Edmonds, H.N., German, C.R., 2004. Particle geochemistry on the Rainbow hydrothermal plume, Mid-Atlantic Ridge. Geochim. Cosmochim. Acta 4, 759–772.

Farley, K.J., Dzombak, A.D., Morel, F.M.M., 1985. A surface precipitation for the adsorption of cations on metal oxides. J. Colloid Interface Sci. 106, 226–242.

Feely, R.A., Lewison, M., Massoth, G.J., Robert-Baldo, G., Lavelle, J.W., Byrne, R.N., Von Damm, K.L., Curl, H.C., 1987. Composition and dissolution of black smoker particles from active vents on the Jaun de Fuca Ridge. J. Geophys. Res. 92, 11347–11363.

Feely, R.A., Massoth, G.J., Baker, E.T., Cowen, J.P., Lamb, M.F., Krogslund, K.A., 1990a. The effect of hydrothermal processes on mid water phosphorous distributions in the North East Pacific. Earth Planet. Sci. Lett. 96, 305–318.

Feely, R.A., Geiselman, T.L., Baker, E.T., Massoth, G.J., Hammond, S.R., 1990b. Distribution and composition of buoyant and non buoyant hydrothemal plume particles from ASHES vent at Axial Volcano, Juan de Fuca Ridge. J. Geophys. Res. 95, 12855–12874.

Feely, R.A., Massoth, G.J., Baker, E.T., Lebon, G.T., Geiselman, T., 1992. Tracking the dispersal of hydrothermal plumes from the Juan de Fuca Ridge using suspended matter composition. J. Geophys. Res. 97, 3457–3468.

Feely, R.A., Massoth, G.J., Trefry, J.H., Baker, E.T., Paulson, A.J., Lebon, G.T., 1994. Composition and sedimentation of hydrothermal plume particles from North Cleft sediment, Juan de Fuca Ridge. J. Geophys. Res. 99, 4985–5006.

Feely, R.A., Baker, E.T., Marumo, K., Urabe, T., Ihibashi, J., Gendron, J., Lebon, G.T., Okamura, K., 1996. Hydrothermal plume particles and the dissolved phosphate over the superfast-spreading southern East Pacific Rise. Geochim. Cosmochim. Acta 60, 2297–2323.

Feely, R.A., Trefry, J.H., Lebon, G.T., German, C.R., 1998. The relationship between P/Fe and V/Fe ratios in hydrothermal precipitates and dissolved in phosphate in seawater. Geophys. Res. Lett. 25, 2253–2256.

Ford, R.G., Bertsch, P.M., Seaman, J.C., 1997. Changes in transition metal and heavy metal partitioning during hydrous iron oxide aging. Environ. Sci. Technol. 31, 2028–2033.

Ford, R.G., Kemner, K.M., Bertsch, P.M., 1999. Influence of sorbate–sorbent interactions on the crystallization kinetics of nickel– and lead–ferrihydrite coprecipitates. Geochim. Cosmochim. Acta 63, 39–48.

Frenz, M., Baumann, K.-H., Boeckel, B., Höppner, R., Henrich, R., 2005. Quantification of foraminifer and coccolith carbonate in south Atlantic surface sediments by means of carbonate grain-size distributions. J. Sediment. Res. 75, 464–475.

Froelich, P.N., Klinkhammer, G.P., Bender, M.L., Luedtke, N.A., Heath, G.R., Cullen, D., Dauphin, P., Hammond, D., Hartman, B., Maynard, V., 1979. Early oxidation of organic matter in pelagic sediments of the eastern equatorial Atlantic: suboxic diagenesis. Geochim. Cosmochim. Acta 43, 1075–1090.

German, C.R., Sparks, R.S.J., 1993. Particle recycling in the TAG hydrothermal plume. Earth Planet. Sci. Lett. 116, 129–134.

German, C.R., Von Damm, K.L., 2003. Hydrothermal processes, In: Elderfield, H., (Ed.), The Oceans and Marine Geochemistry: H.D. Holland and K.K. Turekian (Eds.), Volume 6 Treatise on Geochemistry. Elsevier-Pergamon, Oxford, pp. 145–180.

German, C.R., Klinkhammer, G.P., Edmond, J.M., Mitra, A., Elderfield, H., 1991a. Hydrothermal scavenging at the Mid-Atlantic Ridge: radionuclide distributions. Earth Planet. Sci. Lett. 105, 170–181.

German, C.R., Campbell, A.C., Edmond, J.M., 1991b. Hydrothermal scavenging at the Mid-Atlantic Ridge: modification of trace element dissolved fluxes. Earth Planet. Sci. Lett. 107, 101–114.

German, C.R., Colley, S., Palmer, M.R., Khripounoff, A., Klinkhammer, G.P., 2002. Hydrothermal sediment trap fluxes: 13°N, East Pacific Rise. Deep-Sea Res. I 49, 1921–1940.

Gerth, J., 1990. Unit-cell dimensions of pure and trace-metal associated goethites. Geochim. Cosmochim. Acta 54, 363–371.

Glasauer, S., Weidler, P.G., Langley, S., Beveridge, T.J., 2003. Controls on Fe reduction and mineral formation by a subsurface bacterium. Geochim. Cosmochim. Acta 67, 1277–1288.

Glasby, G.P., 2006. Manganese: predominant role of nodules and crusts, In: Schulz, H.D., Zabel, M. (Eds.), Marine Geochemistry, second edition. Springer-Verlag, Berlin, pp. 371–428.

Grevemeyer, I., Renard, V., Jennrich, C., Weigel, W., 1997. Seamount abundances and abyssal hill morphology on the eastern flank of the East Pacific Rise at 14°S. Geophys. Res. Lett. 24, 1955–1958.

Grevemeyer, I., Weigel, W., Jennrich, C., 1998. Structure and ageing of oceanic crust at 14°S on the East Pacific Rise. Geophys. J. Int. 135, 573–584.

Grevemeyer, I., Schramm, B., Devey, C.W., Wilson, D.S., Jochum, B., Hauschild, J., Aric, K., Villinger, H.W., Weigel, W., 2002. A multibeam-sonar, magnetic and geochemical flowline survey at 14°14′S on the East Pacific Rise: insights into the fourth dimension of ridge crest segmentation. Earth Planet. Sci. Lett. 199, 359–372.

Halbach, P., Scherhag, C., Hebisch, U., Marchig, V., 1981. Geochemical and mineralogical control of different genetic types of deep-sea nodules from the Pacific Ocean. Miner. Depos. 16, 59–84.

Harder, H., 1976. Nontronite synthesis at low temperatures. Chem. Geol. 1, 169–180.

Hauschild, J., Grevemeyer, I., Kaul, N., Villinger, H., 2003. Asymmetric sedimentation on young ocean floor at the East Pacific Rise, 15°S. Mar. Geol. 193, 49–59.

Heath, G.R., Dymond, J., 1977. Genesis and transformation of metalliferous sediments from the East Pacific Rise, Bauer Deep, and Central Basin northwest Nazca plate. Geol. Soc. Amer. Bull. 88, 723–733.

Heath, G.R., Dymond, J., 1981. Metalliferous sediment deposition in time and space: East Pacific Rise and Bauer Basin, northern Nazca plate. Geol. Soc. Am. Mem. 154, 175–197.

Jambor, J.L., Dutrizac, J.E., 1998. Occurrence and constitution of natural and synthetic ferrihydrite, a widespread iron oxyhydroxide. Chem. Rev. 98, 2549–2585.

James, R.H., Elderfield, H., 1996. Dissolved and particulate trace metals in hydrothermal plumes at the Mid-Atlantic Ridge. Geophys. Res. Lett. 23, 3499–3502.

Jeandel, C., Caisso, M., Minster, J.F., 1987. Vanadium behaviour in the global ocean and in the Mediterranean Sea. Mar. Chem. 21, 51–74.

Kastner, M., 1986. Mineralogy and diagenesis of sediments at Site 597; preliminary results. In: Leinen, M., Rea, D.K., et al. (Eds.), Initial Reports of the Deep Sea Drilling Project 92. US Government Printing Office, Washington, pp. 345–349.

Kennedy, C.B., Scott, S.D., Ferris, F.G., 2004. Hydrothermal phase stabilization of 2-line ferrihydrite by bacteria. Chem. Geol. 212, 269–277.

Kennett, J.P., 1982. Marine Geology. Prentice Hall, New Jersey. 813 pp.

Koschinsky, A., Hein, J.R., 2003. Uptake of elements from seawater by ferromanganese crusts: solid-phase associations and seawater speciation. Mar. Geol. 198, 331–351.

Lilley, M.D., Feely, R.A., Trefry, J.H., 1995. Chemical and biochemical transformations in hydrothermal plumes. In: Humphris, S.E., Zierenberg, A., Mullineaus, L.S., Thomson, R.E. (Eds.), Seafloor Hydrothermal Systems: Physical, Chemical, Biological and Geological Interactions. Geophys. Monogr., Am. Geophys. Union, vol. 91, pp. 369–391.

Lupton, J.E., 1995. Hydrothermal plumes: near and far field. In: Humphris, S.E., Zierenberg, A., Mullineaus, L.S., Thomson, R.E. (Eds.), Seafloor Hydrothermal Systems: Physical, Chemical, Biological and Geological Interactions. Geophys. Monogr., Am. Geophys. Union, vol. 91, pp. 317–343.

Mandernack, K.W., Tebo, B.M., 1993. Manganese scavenging and oxidation at hydrothermal vents and in vent plumes. Geochim. Cosmochim. Acta 57, 3907–3923.

Marchig, V., Gundlach, H., 1982. Iron-rich metalliferous sediments on the East Pacific Rise: prototype of undifferentiated metalliferous sediments on divergent plate boundaries. Earth Planet. Sci. Lett. 58, 361–382.

Marchig, V., Erzinger, J., Heinze, P.M., 1986. Sediments in the black smoker area of the East Pacific Rise (18.5° S). Earth Planet. Sci. Lett. 79, 93–106.

Martin, J.H., Gordon, R.M., Fitzwater, S., Broenkow, W.W., 1989. VERTEX: phytoplankton/iron studies in the Gulf of Alaska. Deep-Sea Res. 36, 649–680.

Martinez, C.E., McBride, M.B., 1998. Coprecipitates of Cd, Cu, Pb and Zn in iron oxides: solid phase transformation and metal solubility after aging and thermal treatment. Clays Clay Miner. 46, 537–545.

McManus, J., Nagler, T.F., Siebert, C., Wheat, C.G., Hammond, D.E., 2002. Oceanic molybdenum isotope fractionation: diagenesis and hydrothermal ridge-flank alteration. Geochem. Geophys. Geosyst. 3 art. no. 1078.

Metz, S., Trefry, J.H., 1993. Field and laboratory studies of metal uptake and release by hydrothermal precipitates. J. Geophys. Res. 98, 9661–9666.

Metz, S., Trefry, J.H., Nelson, T.A., 1988. History and geochemistry of a metalliferous sediment core from the Mid-Atlantic Ridge at 26°N. Geochim. Cosmochim. Acta 52, 2369–2378.

Milliman, J.D., Troy, P.J., Balch, W.M., Adams, A.K., Li, Y.-H., Mackenzie, F.T., 1999. Biologically mediated dissolution of calcium carbonate above the chemical lysocline? Deep-Sea Res. 46, 1653–1669.

Mills, R.A., Elderfield, H., 1995. Hydrothermal activity and the geochemistry of metalliferous sediment. In: Humphris, S.E., Zierenberg, A., Mullineaus, L.S., Thomson, R.E. (Eds.), Seafloor Hydrothermal Systems: Physical, Chemical, Biological and Geological Interactions. Geophys. Monogr., Am. Geophys. Union, 91, pp. 392–405.

Morford, J.L., Emerson, S., 1999. The geochemistry of redox sensitive trace metals in sediments. Geochim. Cosmochim. Acta 63, 1735–1750.

Murray, R.W., 1979. Iron oxides. In: Burns, R.G. (Ed.), Marine Minerals, vol. 6. Min. Soc. Am, Washington, DC, pp. 47–98.

Murray, R.W., Leinen, M., 1996. Scavenged excess aluminium and its relationship to bulk titanium in biogenic sediment from the central equatorial Pacific Ocean. Geochim. Cosmochim. Acta 60, 3869–3878.

Murray, R.W., Leinen, M., Isern, A.R., 1993. Biogenic flux of Al to sediment in the Central Equatorial Pacific Ocean: evidence for increased productivity during glacial episodes. Paleoceanography 8, 651–670.

Rudnicki, M.D., Elderfield, H., 1993. A chemical model of the buoyant and neutrally buoyant plume above TAG vent field, 26°N, Mid-Atlantic Ridge. Geochim. Cosmochim. Acta 57, 2939–2957.

Savenko, A.V., 2001. Coprecipitation of manganese, copper, zinc, lead and cadmium with iron hydroxide in hydrothermal plumes (by the data of laboratory modeling). Oceanology 41, 502–507.

Schaller, T., Morford, J., Emerson, S.R., Feely, R.A., 2000. Oxyanions in metalliferous sediments: tracers for paleoseawater metal concentrations? Geochim. Cosmochim. Acta 63, 2243–2254.

Scheirer, D.S., MacDonald, K.C., 1993. The variation in cross-sectional area of the axial ridge along the East Pacific Rise: evidence for the magmatic budget of a fast-spreading ridge. J. Geophys. Res. 98, 2239–2259.

Schramm, B., Devey, C.W., Gillis, K.M., Lackschewitz, K., 2005. Low temperature alteration of basalts during the last 9 Ma at 14°15′S at the Southern East Pacific Rise. Chem. Geol. 218, 281–313.

Schwertmann, U., Murad, E., 1983. Effect of pH on the formation of goethite and hematite from ferrihydrite. Clays Clay Miner. 31, 277–284.

Schwertmann, U., Stanjek, H., Becher, H.-H., 2004. Long-term in vitro transformation of 2-line ferrihydrite to goethite/hematite at 4, 10, 15 and 25 °C. Clay Miner. 39, 433–438.

Severmann, S., Mills, R.A., Palmer, M.R., Telling, J., Cragg, B.A., Parkes, R.J., 2006. The role of prokaryotes in subsurface weathering of hydrothermal sediments: a combined geochemical and microbiological investigation. Geochim. Cosmochim. Acta 244, 170–185.

Shimmield, G.B., Price, N.B., 1986. The behaviour of molybdenum and manganese during early sediment diagenesis – offshore Baja California, Mexico. Mar. Chem. 19, 261–280.

Shimmield, G.B., Price, N.B., 1988. The scavenging of U, ^{230}Th and ^{231}Pa during pulsed hydrothermal activity at 20°S, East Pacific Rise. Geochim. Cosmochim. Acta 5, 669–677.

Smith, C.R., Berelson, W., DeMaster, D.J., Dobbs, F.C., Hammond, D., Hoover, D.J., Pope, R.H., Stephens, M., 1997. Latitudinal variations in benthic processes in the abyssal equatorial Pacific: control by biogenic particle flux. Deep-Sea Res. II 44, 2295–2317.

Speer, K.G., Maltrud, M.E., Thurnherr, A.M., 2003. A global view of dispersion on the Mid-Ocean Ridge. In: Halbach, P., Tunnicliffe, V., Hein, J. (Eds.), Energy and Mass Transfer in Marine Hydrothermal Systems. Dahlem University Press, Berlin, pp. 287–302.

Stanley Jr., J.K., Byrne, R.H., 1990. Inorganic complexation of Zinc (II) in seawater. Geochim. Cosmochim. Acta 54, 753–760.

Tebo, B.M., Bargar, J.R., Clement, B.G., Dick, G.J., Murray, K.J., Parker, D., Verity, R., Webb, S.M., 2004. Biogenic manganese oxides: properties and mechanisms of formation. Annu. Rev. Earth Planet. Sci. 32, 287–328.

Towe, K.M., Bradley, W.F., 1967. Mineralogical constitution of colloidal 'hydrous ferric oxides'. J. Colloid Interface Sci. 24, 384–392.

Trefry, J.H., Metz, S., 1989. Role of hydrothermal precipitates in the geochemical cycling of vanadium. Nature 342, 531–533.

Trocine, R.P., Trefry, J.H., 1988. Distribution and chemistry of suspended particles from an active hydrothemal vent site on the Mid-Atlantic Ridge at 26°N. Earth Planet. Sci. Lett. 88, 1–15.

Varnavas, S.P., 1988. Hydrothermal metallogenesis at the Wilkes Fracture Zone – East Pacific Rise intersection. Mar. Geol. 79, 77–103.

Villinger, H., Grevemeyer, I., Kaul, N., Hauschild, J., Pfender, M., 2002. Hydrothermal heat flux through aged oceanic crust: where does the heat escape? Earth Planet. Sci. Lett. 202, 159–170.

Vorlicek, T.P., Kahn, M.D., Kasuya, Y., Helz, G.R., 2004. Capture of molybdenum in pyrite-forming sediments: role of ligand-induced reduction by polysulfides. Geochim. Cosmochim. Acta 68, 547–556.

Weigel, W., Grevemeyer, I., Kaul, N., Villinger, H., Lüdmann, T., Wong, H.K., 1996. Aging of oceanic crust at the southern East Pacific Rise. EOS Trans. Am. Geophys. Union 77, 504.

Wilson, T.R.S., Thomson, J., Colley, S., Hydes, D.J., Higgs, N.C., Sorensen, J., 1985. Early organic diagenesis: the significance of progressive subsurface oxidation fronts in pelagic sediments. Geochim. Cosmochim. Acta 49, 811–822.